Colloids and Surfaces B: Biointerfaces 255 (2025) 114875

Contents lists available at ScienceDirect

Colloids and Surfaces B: Biointerfaces

journal homepage: www.elsevier.com/locate/colsurfb

pH-responsive chitosan-sodium alginate nanocarriers for curcumin delivery against brain cancer

Salar Mohammadi Shabestari [a], Mehrab Pourmadadi [b,c,*], Hamidreza Abdouss [a], Taranom Ghanbari [d], Majid Abdouss [e], Abbas Rahdar [f,**], Adriana Cambón [g], Pablo Taboada [g,**]

[a] Department of Polymer, School of Chemical Engineering, College of Engineering, University of Tehran, Tehran, Iran
[b] Protein Research Center, Shahid Beheshti University, GC, Tehran 1983963113, Iran
[c] Student Research Committee, Department of Tissue Engineering and Applied Cell Sciences, School of Advanced Technologies in Medicine, Shahid Beheshti University of Medical Sciences, Tehran, Iran
[d] Polymer Reaction Engineering Department, Faculty of Chemical Engineering, Tarbiat Modares University, P.O. Box 14155-143, Tehran, Iran
[e] Department of Chemistry, Amirkabir University of Technology, Tehran, Iran
[f] Department of Physics, University of Zabol, Zabol, Iran
[g] Colloids and Polymers Physics Group, Particle Physics Department, Materials Institute (IMATUS) and Health Research Institute (IDIS), Universidade de Santiago de Compostela, Santiago de Compostela 15782, Spain

ARTICLE INFO

Keywords:
Chitosan/sodium alginate-based nanoparticles
Cerium oxide
Curcumin
Brain cancer

ABSTRACT

Curcumin (CUR) exhibits potent anticancer properties and has been widely investigated for the treatment of various malignancies. However, its clinical application is limited by poor aqueous solubility, rapid systemic metabolism, and a short circulation half-life. In the present study, a pH-responsive hybrid nanocarrier system was developed based on sodium alginate (SA), chitosan (CS), and cerium oxide (CeO_2) nanoparticles (NPs), using a water-in-oil-in-water (W/O/W) double emulsion technique. This system was designed to enhance CUR stability, enable controlled and sustained release, and improve pharmacokinetic parameters such as half-life and biodistribution. The resulting nanocarriers exhibited spherical morphology with textured surfaces, a positive surface charge, and nanoscale dimensions. Structural characterization via XRD and FTIR confirmed a quasi-amorphous composite matrix and successful encapsulation of CUR, achieving an encapsulation efficiency of approximately 86 %. Drug release studies conducted at physiological and acidic pH demonstrated a sustained, pH-dependent release profile, well-fitted by the Baker–Lonsdale kinetic model. Cytotoxicity assays using U-87MG2 glioma and healthy astrocyte cell lines indicated that the CUR-loaded nanocarriers selectively induced tumor cell death while exhibiting minimal toxicity toward normal cells. Moreover, the inclusion of CeO_2 NPs was found to mitigate CUR degradation under physiological conditions, thereby contributing to its enhanced therapeutic performance. Flow cytometry analysis further revealed a significant induction of apoptosis in glioma cells treated with the CUR-loaded nanocomposites. Collectively, these findings underscore the potential of the developed CS/SA/CeO_2@CUR nanoplatform as an effective and biocompatible strategy for brain cancer therapy.

1. Introduction

Cancer continues to represent one of the most significant health challenges worldwide, with brain tumors posing special difficulties due to their complex nature and poor treatment outcomes [1]. According to the World Health Organization, this type of tumors accounts for 1.6 % of all malignancies and 2.5 % of cancer-related deaths [2]. Gliomas represent the most common and aggressive type of brain cancer, accounting for approximately 30 % of all brain malignancies. Due to their elevated recurrence rate, invasive behavior, and poor prognosis [3], gliomas have shown substantial resistance to conventional treatment approaches, including surgery, chemotherapy, and radiotherapy, which

* Corresponding author at: Protein Research Center, Shahid Beheshti University, GC, Tehran 1983963113, Iran.
** Corresponding authors.
E-mail addresses: salarmohammadishabestari@gmail.com (S.M. Shabestari), mehrabpourmadadi@gmail.com (M. Pourmadadi), hamidrezaabdouss@gmail.com (H. Abdouss), taranom.ghanbari@gmail.com (T. Ghanbari), phdabdouss44@aut.ac.ir (M. Abdouss), a.rahdar@uoz.ac.ir (A. Rahdar), adriana.cambon.freire@usc.es (A. Cambón), pablo.taboada@usc.es (P. Taboada).

https://doi.org/10.1016/j.colsurfb.2025.114875
Received 21 March 2025; Received in revised form 3 June 2025; Accepted 7 June 2025
Available online 9 June 2025

are frequently associated with severe side effects. Additionally, their invasive and infiltrative nature, resistance to treatment, and the presence of physiological barriers like the blood-brain barrier (BBB) further complicate the administration of therapeutic agents to the tumor site, limiting the effectiveness of current therapies [4–7].

In this context, nanomedicine has emerged as a promising interdisciplinary field offering novel therapeutic alternatives across cancer treatment and tissue engineering applications [8]. Nanodrug delivery systems (NDDSs), in particular, confer substantial advantages over traditional therapeutic strategies [9–10], such as enhanced biodistribution, controlled pharmacokinetic profiles, and precise site-specific delivery to tumor tissues [11–13], thereby minimizing side effects while improving therapeutic outcomes. This approach not only minimizes side effects but also enables the simultaneous administration of multiple therapeutic agents, potentially generating synergistic effects [14–16]. However, challenges related to biocompatibility, solubility, stability, and scalability of these systems still need to be addressed to fully unlock their therapeutic potential [17,18].

In this regard, natural biomaterials such as chitosan (CS) and sodium alginate (SA) have garnered significant attention in the development of NDDSs due to their outstanding physicochemical and biological properties [19–20]. CS, a biopolymer derived from chitin found in crustacean shells, fungal cell walls, and insect exoskeletons [21,22], exhibits unique characteristics including pH sensitivity, biocompatibility, and mucoadhesiveness [23]. In parallel, SA, a naturally occurring hydrophilic and biodegradable polysaccharide extracted from seaweed, is renowned for its gel-forming capacity and compatibility with a wide range of bioactive molecules [24,25]. The combination of these biopolymers with cerium oxide (CeO_2) nanoparticles not only enhances drug loading and encapsulation efficiency but also introduces additional functionalities such as antioxidant and antibacterial properties [26–27], which can contribute to tumor suppression while preserving healthy tissues. Therefore, the integration of CS, SA, and CeO_2 NPs into a single NDDS—fabricated via a green and scalable synthesis approach—holds great potential for constructing pH-responsive nanocarriers capable of controlled, site-specific drug release in the acidic tumor microenvironment, thereby improving curcumin bioavailability and minimizing systemic side effects [28–30].

Curcumin (CUR), a natural polyphenolic compound extracted from the rhizomes of *Curcuma longa*, has attracted considerable attention for its broad-spectrum anticancer activity, with proven efficacy against brain, breast, colorectal, and prostate malignancies [31]. However, despite its therapeutic promise, the clinical translation of CUR remains significantly limited due to several inherent drawbacks, including poor aqueous solubility, rapid systemic metabolism, low bioavailability, and a short biological half-life of approximately three hours [32–34]. These pharmacokinetic challenges restrict its accumulation at the tumor site and diminish its therapeutic effectiveness. Conventional drug delivery methods have largely failed to overcome these limitations, thereby underscoring the urgent need for advanced NDDSs capable of improving CUR solubility, prolonging circulation time, and facilitating targeted tumor delivery. While several studies have independently explored CS/SA-based nanocarriers, CUR formulations, or CeO_2 nanoparticles for diverse biomedical applications, the combination of these components into a unique, pH-responsive platform specifically designed for brain cancer therapy appears largely unexplored.

Hence, this study aims to develop an innovative, pH-responsive NDDSs capable of efficiently encapsulating CUR by harnessing the synergistic properties of CS, SA, and CeO_2 nanoparticles. The nanocomposite is synthesized via a green, scalable water-in-oil-in-water (W/O/W) double emulsion technique, specifically engineered to exhibit differential drug release under physiological (pH 7.4) and tumor-like acidic conditions (pH 5.4), thereby enabling targeted delivery for effective glioma therapy. This system enhances CUR's aqueous stability and bioavailability, prolongs its biological half-life, and minimizes off-target toxicity through controlled and sustained release. Moreover, the eco-friendly fabrication approach highlights the relevance of green chemistry in advancing cost-effective, biocompatible platforms for brain cancer therapeutics.

By addressing critical gaps in existing research, this work provides a comprehensive evaluation of the physicochemical characteristics, stability, and anticancer effects of the developed nanocomposite. The findings present a significant step forward in the development of efficient, targeted, and eco-friendly drug delivery systems, offering a promising avenue for improving therapeutic outcomes in cancer treatment, particularly in the management of brain tumors.

2. Methodology

2.1. Materials

Sodium alginate, chitosan with a 75 % deacetylation degree (M_w = 50 kDa), ethanol, curcumin, 3-(4,5- dimethylthiazol-2-yl)-2,5-diphenyl-2H-tetrazolium bromide (MTT), acetic acid, span-80 surfactant. Specific dialysis tubing, annexin V-fluorescein isothiocyanate (FITC), propidium iodide (PI), dimethylsulfoxide (DMSO), and phosphate buffer saline solution (PBS) were from Sigma Aldrich (USA). Cerium oxide NPs were purchased from Merck (USA). These NPs exhibit spherical morphology with an average particle size in the range of 9–20 nm [27]. Sesame oil was purchased from Niri products (Iran). 0.25 % (w/v) trypsin and 0.1 % (w/v) ethylene diamine tetraacetic acid (EDTA) were from Sunbio (Beijing Solarbio Science and Technology, China) Fetal bovine serum (FBS) and high glucose Dulbecco's Modified Eagle's Medium (DMEM) were from Thermo Scientific and Gibco-Life Technologies, respectively. U-87MG2 human brain cancer and healthy astrocyte cells were obtained from the Iranian Pasteur Institute. Materials were used as received.

2.2. Fabrication of drug-loaded hydrogel solution

To fabricate CUR-containing nanocarriers, a drug-loaded hydrogel solution was initially prepared as follows: First, CS powder was mixed with 2 % (v/v) acetic acid to create a 2 % (w/v) CS solution. Subsequently, SA powder was dissolved in the CS solution, resulting in a final SA concentration of 1 % (w/v). After sonication of the polymer mixture for 10 min, 40 mg of CeO_2 NPs were dissolved in the mixed solution. Next, a CUR solution was introduced into the hybrid polymeric dispersion and stirred for 30 min. For a final CUR concentration of 5 μg/mL in 100 mL of polymeric solution, 0.5 mL of CUR solution with an initial concentration of 1 mg/mL was added. At this stage, a gel-like solution of CS/SA/CeO_2 loaded with CUR was formed.

2.3. Nanocarrier synthesis

Span 80 was introduced into the CUR-loaded hydrogel solution at a concentration of 0.2 % (v/v). For a hydrogel volume of 100 mL, this corresponds to 0.2 mL of Span 80. The mixture was briefly stirred to ensure proper dispersion. Span 80-containing solution was then slowly introduced into sesame oil at a volume ratio of 1:3 and stirred vigorously for 15 min, resulting in the formation of a water-in-oil (W_1/O) emulsion. A second aqueous phase (W_2) was progressively added to this initial emulsion at a volume ratio of 3:4 under continuous vigorous stirring for 30 min in order to produce a water-in-oil-in-water ($W_1/O/W_2$) emulsion. Span 80 was used as the stabilizer to maintain the stability of both the W_1/O and $W_1/O/W_2$ emulsions, preventing phase separation.

After stirring, the emulsion was left undisturbed for 10 min to allow distinct layers to phase separate (oil phase, water phase, and the phase containing the nanocarriers). The oil phase was carefully extracted using a pipette avoiding disturb the other layers. The remaining phase containing the nanocarriers was subjected to centrifugation at 5000 rpm for 10 min, resulting in the sedimentation of the nanocarriers at the bottom of the tube. The supernatant was discarded, and the collected nanocarriers were subjected to freeze-drying to remove residual water. The resultant powder was stored in a refrigerator for future use. This powder

was designated as CS/SA/CeO_2@CUR (See Scheme 1).

2.4. Characterization of drug-loaded nanocarriers

The size, stability and morphology of CUR-loaded nanocarriers were analyzed through dynamic light scattering, DLS, (Nanosize XS Nano, Malvern, UK) and FE-SEM (Mira3, Tescan, Czech Republic), respectively. Prior to FE-SEM imaging, the nanocarriers underwent gold coating to enhance conductivity. The images were captured at different magnifications (accelerating voltage 20 kV). To analyze the chemical interactions between the polymers and CUR within the nanocarriers, FTIR (Perkin Elmer, USA) was employed. FTIR spectra were collected within the range of 500–4000 cm^{-1} (resolution of 1 cm^{-1}), using 32 scans for signal averaging to enhance spectral quality. Additionally, XRD (Bruker D8 Advance, Germany) was made to determine the nanocarriers crystalline structure. The XRD patterns were recorded in a 2θ range between 5° and 80° (scanning rate = 0.02°/s), using CuKα radiation of λ = 1.5406 Å. The nanocarrier particle size, polydispersity index (PDI), and surface charge were assessed through DLS and ZP analyses, using a SZ-100z analyzer (Horiba, Japan). The nanocarriers were sonicated in aqueous solution before measurements, and experiments were performed at 25 °C at least in triplicate.

For all quantitative measurements made for characterization and biological assays, data were reported as mean ± standard deviation (SD) with at least three independent replicates.

2.5. Drug loading and encapsulation efficiency

1 mg of CUR-loaded nanocarriers was dispersed in 1 mL of PBS. After the addition of 1 mL of ethyl acetate (to dissolve any unencapsulated CUR), the optical density (OD) of the obtained solution was measured at 419 nm. The absorbance readings were then used to calculate the drug concentration based on a calibration curve for CUR. CUR EE% and LE% were determined using Eq (1) and (2) [35,36]:

$$EE(\%) = \frac{w_{t,CUR} - w_{un,CUR}}{w_{t,CUR}} \times 100 \quad (1)$$

$$LE(\%) = \frac{w_{t,CUR} - w_{un,CUR}}{w_{t,NC}} \times 100 \quad (2)$$

where $w_{t,\ CUR}$ is amount of total CUR, $w_{un,\ CUR}$ is amount of unbound CUR, and $w_{t,\ NC}$ is total amount of CUR loaded nanocarriers.

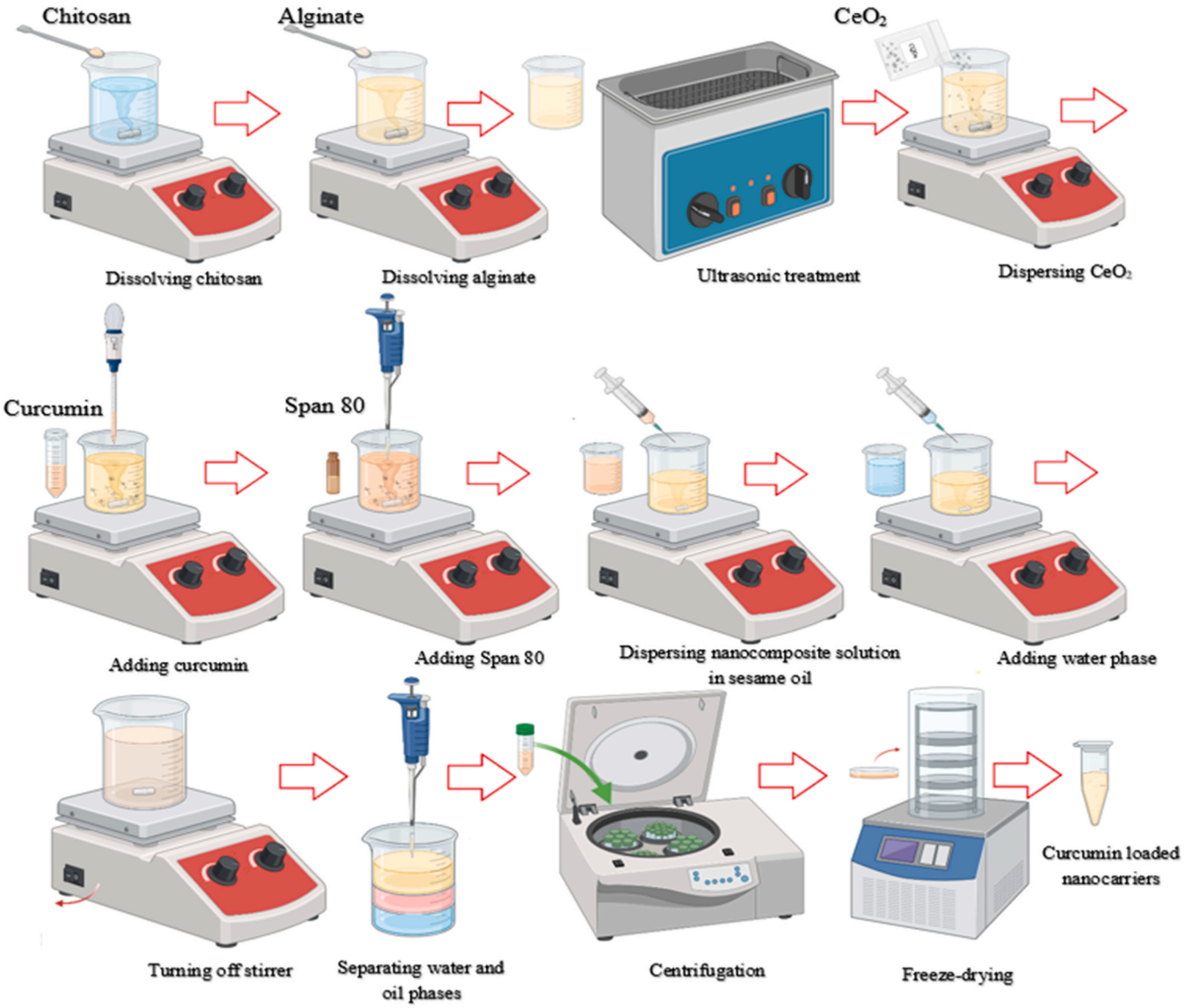

Scheme 1. Scheme depicting the synthetic procedure to obtain the nanoformulation.

2.6. Drug release kinetics

To monitor the time-dependent Cur drug release, nanocarriers containing CUR were dispersed in aqueous media after transferring 5 mL of nanocarrier dispersion into a dialysis bag (MWCO = 12 kDa) and submerged in a tube filled with 30 mL of buffer solution comprising PBS and ethanol in a 4:1 vol ratio. Then, CUR release experiments at different pH values were conducted in buffer solutions at different pH of 5.4, and 7.4. The pH was adjusted by adding appropriate volumes of citric acid and sodium hydroxide solutions. The tubes were then placed at 37 °C and gently agitated. At different time intervals, 300 μL of the release media were collected, and its absorbance at 419 nm was measured. To maintain the volume constant at 30 mL, 300 μL of fresh media were incorporated into the tube after each collection. The absorbance values were then converted into drug concentration using a previously established CUR calibration curve. The drug release (%) was determined by normalizing the released CUR amount to the initially loaded CUR, as indicated in Equation (3) [21]:

$$DR(\%) = \frac{C_r}{C_l} \times 100 \tag{3}$$

where C_r and C_l represent the amount of released CUR and the amount of loaded CUR, respectively.

Next, the experimental release data were fitted to different mathematical models, including Higuchi, Weibull, Korsmeyer-Peppas, Baker-Lonsdale, First-order, Hixson-Crowell, and Zero-order ones. The selection of the most suitable model was based on the assessment of R^2 values.

Zero-order release (Eq. (4)) represents an optimal drug release scenario, characterized by a constant release rate maintained over a specific period [37,38]:

$$M_t = M_0 + K_0 t \tag{4}$$

In this equation, M_t, stands for the cumulative drug amount released at time t, M_0, refers to the initial drug quantity, and K_0 referes to Zero-order constant for Zero-order.

In the First order release model (Eq. (5)), the release rate is not constant, and instead is concentration-dependent. In this model, the release rate decreases with time [39]:

$$lnM_t = lnM_0 + K_1 t \tag{5}$$

where M_t is the cumulative amount of drug released at time t, M_o is the initial amount of drug released, and K_1 is the first-order drug release constant.

In Higuchi model (Eq. (6)), the cumulative drug release follows a pattern that is directly related to the square root of time. This approach effectively explains drug release in matrix systems where the concentration of the drug significantly exceeds its solubility, and matrix dissolution plays a minimal role [39,40]:

$$\frac{M_t}{M_\infty} = K_H \sqrt{t} \tag{6}$$

In this equation, M_∞ is the drug released at infinite time, M_t, stands for the cumulative amount of drug released at time t, and K_H is the constant for Higuchi drug release.

The Hixson–Crowell model (Eq. (7)) describes drug release from nanocarriers in which dissolution is the dominant mechanism. In this model, the surface of the release system decreases over time while its geometry remains unchanged [40]:

$$\sqrt[3]{M_i} - \sqrt[3]{M_r} = K_{HC} t \tag{7}$$

where M_i is the initial quantity of drug in the system, M_r is the amount of drug remaining at time t, and K_{HC} is the Hixson–Crowell release constant.

The Korsmeyer–Peppaś model (Eq. (8) represents a semi-empirical model in which drug release is exponentially related to time. The release mechanism is predicted according to the release exponent: If $n \leq 0.5$, the release is considered mainly governed by diffusion, and if $0.5 < n < 1$, it is mediated by both swelling and diffusion (anomalous transport). For $n = 1$, the swelling is the leading mechanism [41,42]:

$$\frac{M_t}{M_\infty} = Kt^n \tag{8}$$

In this equation, M_t stands for the cumulative drug release at time t, M_∞ refers to the total drug release at infinite time, K represents the Korsmeyer–Peppas release constant, and n is the exponent indicating the release mechanism.

The Baker–Lonsdale model (Eq. (9)) is a modified form of Higuchi expression for spherical matrix systems such as microspheres and microcapsules [41]:

$$\frac{3}{2}\left[1 - \left(1 - \frac{M_t}{M_\infty}\right)^{2/3}\right] - \frac{M_t}{M_\infty} = K_{BL}.t \tag{9}$$

This equation defines M_t as the cumulative drug release at time t, M_∞ as the drug release at infinite time, K_{BL} indicates the rate constant for diffusion.

Finally, the Weibull model (Eq. (10)) is a stretched exponential function predicting drug release from matrix systems in a finite time [43]:

$$\frac{M_t}{M_\infty} = 1 - exp\left[\frac{-(t - T_i)^\beta}{\alpha}\right] \tag{10}$$

In this equation, M_t signifies the cumulative drug release at time t, while M_∞ refers to release amount at infinite time. T_i accounts for the delay in the release process, typically assumed to be 0. Therefore, the equation is expressed as follows [44]:

$$\frac{M_t}{M_\infty} = 1 - e^{-t^{\beta/\alpha}} \tag{11}$$

α and β define timescale of the process and shape of the curve, respectively.

2.7. in vitro cytotoxicity and ROS assessment

To assess the potential cytotoxic effects of CUR-containing nanocarriers, an MTT assay was done. Within living cells, the MTT reagent undergoes conversion into formazan precipitates catalyzed by mitochondrial dehydrogenase enzymes. Higher MTT reduction and increased formazan formation correspond to greater cell viability and reduced cytotoxicity. The assay iwas done using two cell types: a glioblastoma cell line (U-87MG2) and primary astrocytes. Cells were cultivated in DMEM (containing 1 % pen/strep and 10 % FBS). After reaching confluence, cells were washed with PBS, treated with trypsin/EDTA solution for 5 min, and centrifuged at 1500 rpm for 5 min. The collected cells were cultivated in a 96-well plate (5000 cells/well). After 24 h, the culture medium was substituted with 100 μL of each test sample, including free CUR, CS solution, CS/SA blended solution, CS/SA/CeO_2 nanocomposite, and CUR-loaded CS/SA/CeO_2 nanocarriers. A well with cell culture media was used as the control. After incubating the cells for 1, 2, and 3 days, the cell medium were removed, and 100 μL/well of MTT solution was introduced into the plate and incubation was conducted for 4 h, the MTT solution was then removed, and DMSO (100 μL/well) was added. After incubation at 25 °C in the dark for 15 min, the OD was measured at 570 nm by UV-Vis spectrophotometry. Cell viability was calculated using the following equation:

$$Viability(\%) = \frac{A_s}{A_c} \times 100 \tag{12}$$

where A_s and A_c are absorbance of the sample and controls, respectively.

For ROS assessment, the Fluorometric Intracellular ROS kit (Sigma-Aldrich) was used to detect ROS, following the protocol provided by the manufacturer. For this, $1{\cdot}10^4$ cells/well were seeded in 96-well plates (100 μL DMEM without phenol red) and grown for 24 h under standard culture conditions. Subsequently, the different treatments (50 μL) were added and incubated for 23 h. After this time, the medium was discarded, the cells were washed three times with PBS (pH 7.4) and fresh medium without phenol red was added. Then, 100 μL of ROS detection reagent was added to each well and incubated at 37 ºC for 1 h. Bare cells were used as a negative control, and added H_2O_2 (800 μM, 33 % w/v) as the positive one. Finally, the cells were incubated for 30 min. The plates with the samples and controls were measured on a plate reader (FLUOstar OMEGA) at $\lambda_{ex} = 488$ nm and $\lambda_{em} = 535$ nm.

2.8. Flow cytometry

To additionally investigate the cell death mechanism of CUR-loaded nanocarriers, the Annexin V-FITC/PI apoptosis detection kit (A2214-Sigma) was utilized. Initially, U-87MG2 cells were cultivated in a 96-well plate and after incubation for 24 h, 100 μL of each test sample—free CUR, CS solution, CS/SA blend, CS/SA/CeO_2 nanocomposite, and CUR-loaded CS/SA/CeO_2 nanocarriers were introduced to the wells. The control group was maintained with standard cell culture medium. After a 48 h of incubation, the cells were detached using trypsin/EDTA, washed twice with PBS, and subjected to centrifugation. The collected cells (approximately 10^5 cells) were then suspended in 0.5 mL 1X of binding buffer. Afterwards, 5 μL of Annexin V-FITC was introduced into each tube, and these were kept at 4 °C in the dark for 15 min. Then, 1 mL of binding buffer was added, samples centrifuge at 1500 rpm for 5 min, the supernatant discarded, and the cells were suspended in 0.5 mL of fresh binding buffer. Finally, 3 μL of PI was poured to each sample, and finally, flow cytometry analysis (BD FACSCalibur, BD Biosciences, USA) was carried out.

3. Results and discussion

3.1. Nanocarrier characterization

The population size distribution of the developed nanocarriers was assessed by DLS. Fig. 1**A** shows a relatively narrow distribution with a single, well-defined peak centered at 219 nm and a PDI of 0.23, which falls within the optimal size range for nanocarrier-mediated drug delivery [45–48], enabling passive tumor targeting via the EPR effect [49]. The nanocarriers exhibited a positive surface charge of 119.32 mV (Fig. 1**B**), well above the ±30 mV threshold typically associated with colloidal stability driven by electrostatic repulsion [50,51]. The

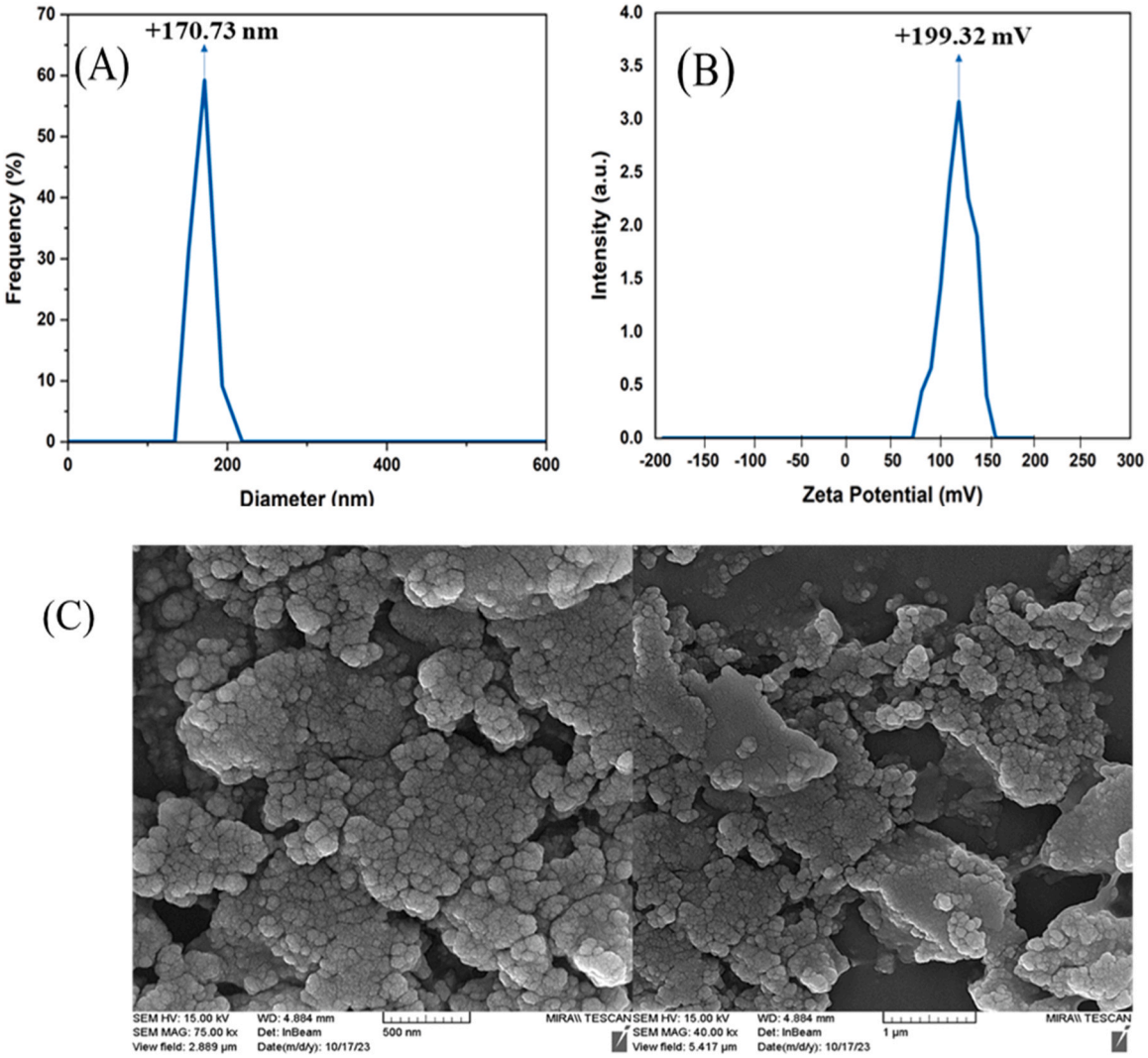

Fig. 1. (A) Particle size distribution, (B) zeta potential; and (C) images of freeze-dried CS/SA/CeO_2@CUR hybrid NPs as observed by FE-SEM.

relatively high zeta potential (+199.3 mV) is primarily attributed to the cationic nature of the CS shell under acidic conditions, which promotes strong intra- and interchain electrostatic repulsion and prevents nanoparticle aggregation during formation [21]. This positive surface charge was intentionally engineered to enhance cellular uptake through electrostatic interactions with negatively charged glioma membranes and to facilitate BBB penetration [4,21]. Although highly cationic systems are known to interact with serum proteins when injected systemically forming a protein biocorona, such shell may be favorable to reduce potential particle cytotoxicity, reduce nonspecific interactions and improve systemic compatibility [50], as confirmed by MTT and flow cytometry assays (Section 3.3). In addition, CeO_2 NPs are hypothesized to act as potential heterogeneous nucleation sites, promoting controlled polymer self-assembly and contributing to make particle core a more suitable environment for drug encapsulation [27].

Notably, the present nanocarriers displayed a higher surface charge than other systems previously reported to encapsulate CUR (Table 1), pointing to a potential superior colloidal stability. The positive zeta potential values also indicate that CS chains are likely to constitute the outermost layer of the nanocarriers, with SA and CeO_2 NPs distributed more internally. In addition, the morphology and size of the CS/SA/CeO_2@CUR NPs were evaluated using FE-SEM (Fig. 1**C**). FE-SEM images revealed nanoparticles with irregularly spherical morphology and an average size of approximately 78 nm, exhibiting textured surfaces that may favor interactions with surrounding biological cells and tissues [49]. Differences in size between DLS and FE-SEM arises from the freeze-drying process done during the preparation of NP samples for imaging, which leads to the shrinking of the external surfactant/polymeric coating layer.

Fig. 2 shows the FTIR spectra of CS/SA/CeO_2@CUR nanoparticles. In all spectra, broad absorption bands between 3220 and 3530 cm^{-1} are observed, corresponding to O–H stretching vibrations. These bands also overlap with N–H stretching vibrations in CS, indicating the presence of extensive intermolecular hydrogen bonding [53].

In the spectrum of pure CS (Fig. 2**A**), a characteristic peak around 2859 cm^{-1} is attributed to C–H stretching vibrations, while a prominent band at 1585 cm^{-1} corresponds to C═O stretching of the secondary amide group (–NHCO–). Additional bands at 1029 and 1380 cm^{-1} are associated with C–O–C and C–N stretching vibrations, respectively [54]. In the case of SA (Fig. 2**B**), a peak at 2940 cm^{-1} reflects C–H stretching, and strong bands at 1592 and 1404 cm^{-1} correspond to the asymmetric and symmetric stretching vibrations of the carboxylate ($–COO^-$) groups [24,55]. The band observed at 1297 cm^{-1} is attributed to C–C–H and O–C–H bending vibrations, while the peaks at 1022 cm^{-1} and 813 cm^{-1} correspond to C–O stretching and Na–O bonding modes, respectively [56]. The spectrum of the CS/SA complex (Fig. 2**C**) exhibits features of both polymers. A new band appearing at 1401 cm^{-1}, absent in pure CS, confirms the presence of carboxylate groups from SA. Furthermore, the broad O–H/N–H stretching band in the region of 3220–3530 cm^{-1} exhibits reduced intensity, indicating the formation of hydrogen bonds and electrostatic interactions between the carboxylate (COO^-) groups of SA and the protonated amine (NH_3^+) groups of CS [57]. The shift of the secondary amide band from 1380 cm^{-1} (in CS) to 1340 cm^{-1} in the complex further supports this interaction [58]. The incorporation of CeO_2 into the polymeric matrix (Fig. 2**D**) is evidenced by the appearance of a distinct band near 560 cm^{-1}, corresponding to Ce–O stretching vibrations, confirming the successful embedding of the inorganic phase [59]. Finally, the spectrum of CS/SA/CeO_2@CUR nanocarriers (Fig. 2**E**) shows a new peak at 1610 cm^{-1}, which corresponds to C═C stretching in the aromatic rings of CUR, confirming its encapsulation [46]. The broad O–H band shifts slightly to 3200–3500 cm^{-1}, indicating enhanced hydrogen bonding. The secondary amide band remains at 1340 cm^{-1}, and the symmetric carboxylate band stabilizes at 1401 cm^{-1}. The asymmetric carboxylate stretching shifts from 1592 cm^{-1} (SA) and 1585 cm^{-1} (CS) to approximately 1580 and 1578 cm^{-1}, respectively. These spectral shifts collectively confirm the presence of strong molecular interactions among CS, SA, CeO_2, and CUR, which contribute to the stability and structural integrity of the nanocarrier system.

Table 1
Zeta potential values of different CUR-loaded NPs and nanocomposites.

Nanocarrier	Zeta potential (mV)	Ref.
Chitosan/polyacrylic acid/g-C_3N_4	+ 46–52	[21]
Gelatin/starch/Fe_3O_4	+ 50	[42]
Polyacrylic acid/carboxymethyl cellulose /halloysite nanotube	+ 36	[51]
Chitosan/agarose/montmorillonite	+ 47	[52]
Chitosan/sodium alginate/cerium oxide	+ 119	This work

XRD analysis was conducted to investigate the crystalline structure and the impact of component interactions within the developed nanocarriers on that. As depicted in Fig. 3, the XRD pattern of pure CS (Fig. 3**A**) exhibits a sharp peak at $2\theta = 20.6°$, assigned to the (110) plane, indicating its semi-crystalline nature due to strong inter- and intramolecular hydrogen bonding [21]. In contrast, SA (Fig. 3**B**) presents two peaks at $2\theta = 13.3°$ and 22°, both of which are significantly less intense than the peak observed for CS. This reflects SA inherently lower crystallinity [60]. When CS and SA are combined (Fig. 3**D**), the peak at 20.6° broadens and decreases in intensity, and SA peaks become less defined or disappear. These changes suggest reduced crystallinity, likely due to disruption of CS hydrogen bonds by electrostatic interactions between the NH_3^+ groups of CS and the COO^- groups of SA.

This structural reorganization points to the formation of a polyelectrolyte complex [61]. The XRD pattern of pure CeO_2 nanoparticles (Fig. 3**C**) displays distinct peaks at $2\theta = 28.6°$, 33.1°, 47.5°, 56.4°, 65.7°, and 75.4°, corresponding to the (111), (200), (220), (311), (222), and (400) planes of the cubic fluorite structure [62]. Upon incorporating CeO_2 into the CS/SA matrix (Fig. 3**E**), the major peaks at 28.6° and 33.1° are retained but slightly shifted (28.6° → 28.3°, 33.1° → 33.4°), while peaks at higher angles become weakened or vanished. This shift and attenuation suggest successful incorporation of CeO_2 within the carrier matrix, leading to lattice distortion and partial amorphization—hallmarks of strong interactions between the polymeric network and the nanoparticles [26]. Following the encapsulation of CUR (Fig. 3**F**), a new diffraction peak emerges at $2\theta = 22.1°$, characteristic of CUR's crystalline form [52], thereby confirming its successful loading. Concurrently, a further reduction in the intensity of CeO_2-related peaks is observed, suggesting additional interactions between CUR and CeO_2 that contribute to an increase of amorphous character and homogeneous drug dispersion. Collectively, the observed XRD patterns confirm the successful formation of the CS/SA/CeO_2@CUR nanocomposite, where each component contributes to the final structural fingerprint. The systematic broadening and intensity reduction of the diffraction peaks—particularly those of CeO_2—indicate partial loss of long-range crystallinity and the formation of a hybrid amorphous–crystalline matrix. This structural transformation is not merely physical but functionally significant: the amorphous nature enhances CUR dispersion within the polymeric network, while the residual crystalline domains aid in maintaining structural integrity. Such dual-phase architecture is particularly favorable for pH-responsive and sustained drug release, as it supports slower diffusion kinetics, prevents burst release, and improves formulation stability. Therefore, the XRD results not only validate the presence and interaction of individual components but also correlate directly with the improved physicochemical behavior of the nanocarrier system in therapeutic applications.

3.2. Colloidal stability and CUR encapsulation and release from hybrid NPs

The nanocarriers were observed to retain their dispersability and

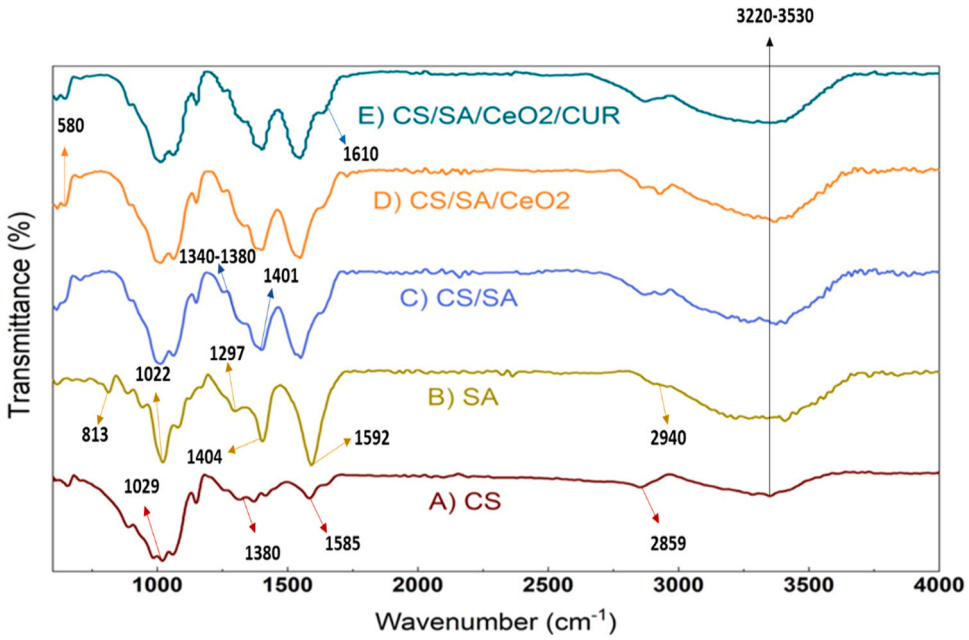

Fig. 2. FTIR spectra of (A) CS, (B) SA, (C) CS/SA, (D) CS/SA/CeO_2, and (E) CS/SA/CeO_2@CUR hybrid NPs.

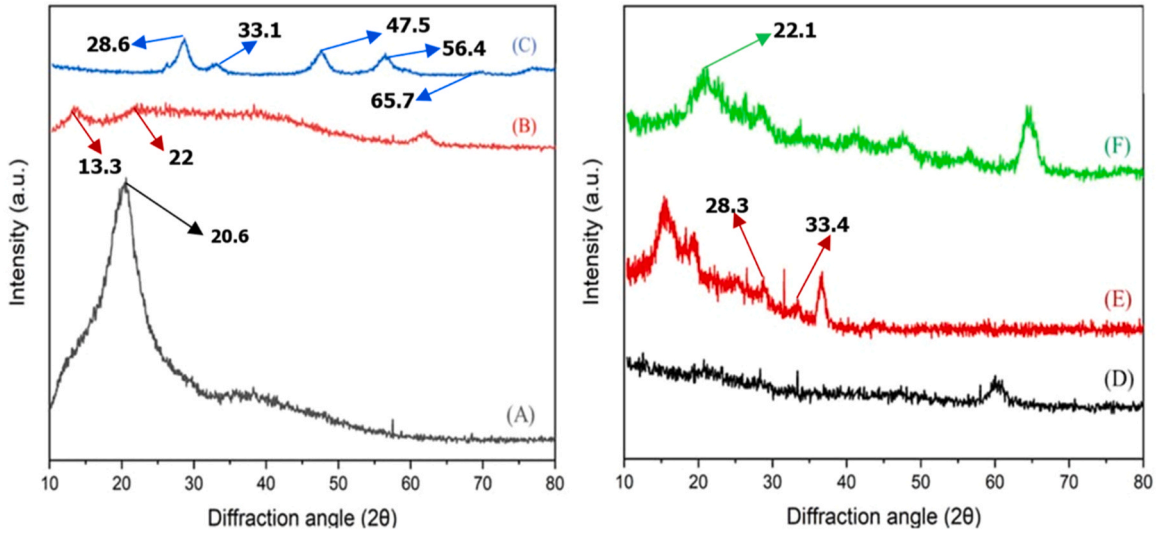

Fig. 3. XRD profiles of (A) CS, (B) SA, (C) CeO_2, (D) CS/SA, (E) CS/SA/CeO_2, and (F) CS/SA/CeO_2@CUR NPs.

surface charge after short-term freezing storage, with no visible aggregation or redispersibility issues as observed from DLS and zeta potential analyses after thawing (not shown). The long-term colloidal stability of the nanoformulation was confirmed by the fact that the particle hydrodynamic diameter was maintained after prolonged incubation in aqueous solution (see Fig. 4**a**). For the first 7 days of incubation, only very slight increases in hydrodynamic diameter of ca. 10 nm were observed which might be related to the existence of some particle swelling and/or formation of some isolated cluster upon dispersion. Nevertheless, no evidence of either aggregation or precipitation were noted, as observed by the naked eye.

On the other hand, the EE and LE of the nanocarrier formulation was also evaluated. CUR encapsulation in CS/SA nanocarriers was evaluated in both the absence and presence of incorporated CeO_2 NPs. In the absence of CeO_2, the EE and LE were 70 % and 35 %, respectively. Upon incorporation of CeO_2, these values increased to 86 % and 49 %, respectively—comparable to those previously reported for other polymer-based systems (Table 2). This enhancement is primarily attributed to interactions such as hydrogen bonding and adsorption between CUR and some potential interfacially located CeO_2 NPs, which do not fully occupy the hydrophobic core but facilitate entrapment near the polymer interface. Such spatial arrangement would promote CUR retention without compromising the whole total internal volume. The nanoscale size and high surface area of CeO_2 particles may also facilitate interactions by providing more accessible binding sites. Additionally, the improved chemical compatibility between CS and SA strengthens matrix integrity, supporting CUR retention, particularly under tumor-mimicking physicochemical stress. Although not directly contributing to drug loading, the CS/SA polymer complex acts as a structural enabler by stabilizing the encapsulated drug and reducing diffusional-loss [63]. π–π stacking interactions between CUR and aromatic moieties of CS and SA [64], as well as hydrogen bonding among hydroxyl and amino groups of CS, hydroxyl groups of CUR, and carboxyl groups of SA, would further support encapsulation, as evidenced by FTIR spectra (Fig. 2).

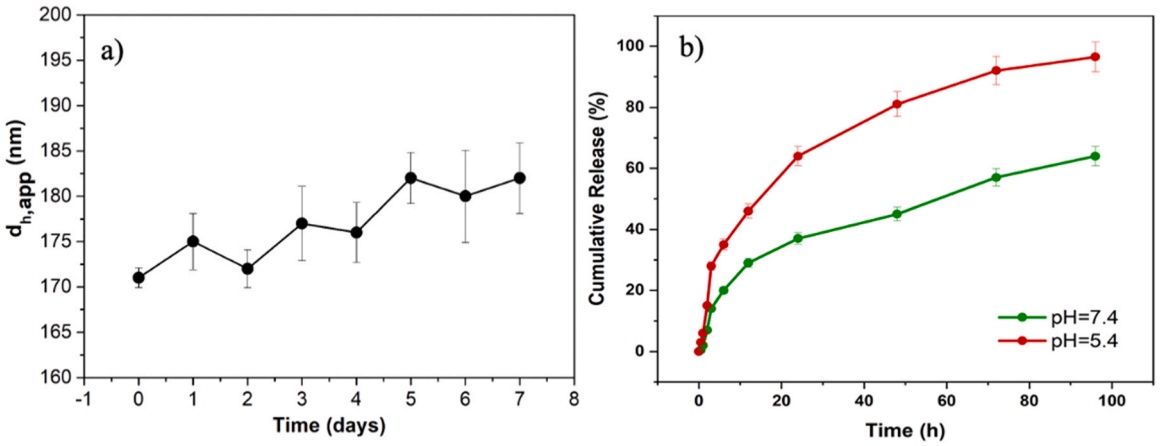

Fig. 4. A) Stability of the nanoformulation along time in aqueous solution. B) cumulative CUR release profiles from the nanocomposites as a function of time at ph 7.4 and 5.4 (red and Green lines, respectively). data are shown as mean ± SD.

Table 2
Drug loading and encapsulation efficiency of various CUR delivery systems with the nanocarrier.

Nanocarrier	Drug encapsulation efficiency (%EE)	Drug loading efficiency (% LE)	Ref.
Zein/ Carboxymethylated/ short chain amylose	34	3.8	[65]
Chitosan/polyacrylic acid/ g-C_3N_4	87	48	[21]
Poly(lactic-co-glycolic acid)	75	6.5	[66]
Polyacrylic acid/ carboxymethyl cellulose/ hallosyte nanotubes	87	45	[51]
CS/SA/CeO_2@CUR	86	49	This work

Importantly, the high EE (86 %) obtained cannot be considered a result of an small initially added drug amount, but rather reflects the carefully optimized encapsulation conditions and the favorable interactions between CUR and the polymer-inorganic matrix. The initial CUR concentration (5 μg/mL) was selected based on pre-formulation trials to avoid aggregation and ensure homogenous dispersion during emulsification [21,38,52]. Furthermore, the high LE value (49 %) confirms that the amount of CUR used was suitable and efficiently entrapped within the nanocarriers.

To evaluate the influence of pH on drug release kinetics, CUR release profiles from the nanocarrier were measured in both acidic and neutral aqueous media, simulating the intratumoral and physiological environments, respectively. Dialysis-based experiments revealed a two-phase release pattern (Fig. 4**b**): an initial burst release within the first 6 h, during which approximately 35 % and 20 % of CUR were released at pH 5.4 and 7.4, respectively, followed by a more sustained release phase. After 15 and 60 h, 50 % of CUR was released under acidic and neutral conditions, respectively, reaching final release values of approximately 96.5 % (pH 5.4) and 64 % (pH 7.4) at 96 h.

The enhanced release under acidic conditions is attributed to the pH-responsive behavior of CS and SA, the primary constituents of the nanocarrier matrix. Both polymers contain ionizable groups whose protonation states are governed by their respective pKa values (approximately 6.5 for CS and 3.4 for SA) [67,68]. At pH values below their pKa, CS primarily presents protonated NH_3^+ groups, while SA bears partially ionized COO^- groups. These pH-dependent surface charges modify electrostatic interactions within the polymer network, significantly impacting matrix swelling and drug diffusivity.

In acidic environments, enhanced protonation of CS leads to increased intra-chain repulsion and loosening of the polymer matrix, promoting water penetration and facilitating accelerated drug diffusion. This behavior has been previously described as a mechanism contributing to the swelling-triggered release response in polyelectrolyte hydrogels [69,70]. Moreover, the mild acidic degradation of CS at pH 5.4 further contributes to matrix destabilization and enhanced CUR release [21].

It is noteworthy that the ionic strength of the release medium was maintained constant (~0.15 M) throughout all experiments to eliminate the influence of different electrostatic screening and only considering the specific influence of pH on matrix behavior and drug diffusivity.

The release profiles were modelled to evaluate the CUR release kinetics from CS/SA/CeO_2@CUR hybrid NPs using several kinetic models for comparison: Hixon-Crowell, Baker-Lonsdale, Korsmeyer-Peppas, Higuchi, first-order, and zero-order. Data analysis presented in Fig. 5 and Table 3 confirmed the Baker-Lonsdale model as the most appropriate to describe the experimental data according to its highest R^2 value. This mathematical model provides evidence that the primary mechanism governing drug release is polymer swelling, in agreement with the experienced release enhancements noted under acidic conditions which is compatible with the stregnthen of electrostatic repulsions of CS chains. The Baker-Lonsdale rate constant (K_{BL}) was higher at pH 5.4 (K_{BL}=0.0040) than at pH 7.4 (K_{BL}=0.0010), further supporting the influence of pH-sensitive polymer swelling on the release behavior. This suggests that the increased drug release in acidic conditions is primarily driven by the structural relaxation and expansion of the polymer matrix, facilitating the diffusion of CUR molecules [42]. The Korsmeyer-Peppas model also provided valuable insights, showing an exponent of 0.36 at pH 5.4 and 0.38 at pH 7.4, respectively. An exponent value below 0.43 indicates that the drug release follows Fickian diffusion, where the process is predominantly governed by the concentration gradient and diffusion through the polymer matrix, resulting in a primarily linear drug release pattern [71]. These findings suggest effective control of drug release, particularly at pH 5.4, where conditions mimic the tumor microenvironment.

3.3. in vitro biocompatibility and therapeutic effect of nanocarriers

The cytotoxicity and therapeutic efficacy of the CS/SA/CeO_2@CUR drug-loaded nanocomposite in suppressing brain tumor cell proliferation were evaluated using the MTT assay on astrocytes and U-87MG2 glioma cells at 24, 48, and 72 h of incubation. As shown in Fig. 6**A**, astrocytes treated with CS, CS/SA, and CS/SA/CeO_2 exhibited high cell viability above 95 % at a polymer concentration of 80 μg/mL, comparable to the untreated control group. Treatment with free CUR (8 μg/mL) and CS/SA/CeO_2@CUR (containing an equivalent amount of CUR)

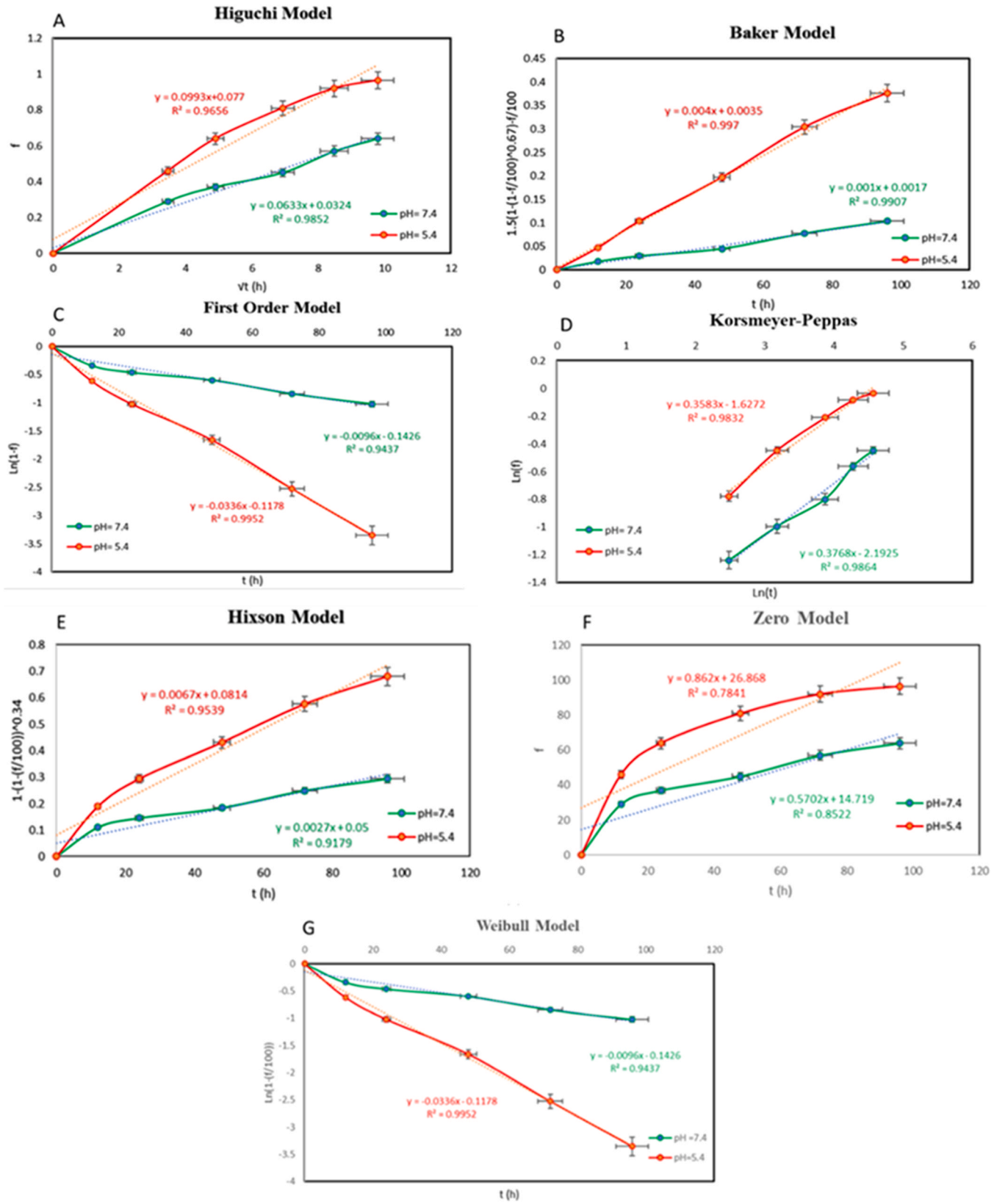

Fig. 5. Drug release data fitted to kinetic models (Green and red lines are related to neutral and acidic pH, respectively). data are shown as mean ± SD.

slightly reduced viability to 89 %, 87 %, and 85 % at 24, 48, and 72 h, respectively, confirming the excellent biocompatibility of the nanocarrier in healthy brain cells.

In U-87MG2 cells (Fig. 6B), free CUR reduced viability to 53 %, 50 %, and 48 % at the same time points, whereas the CUR-loaded nanocarriers achieved slightly greater suppression (54 %, 52 %, and 51 %), indicating sustained therapeutic activity. Although the difference in viability percentages between the two treatments was modest

Table 3
Coefficients of determination upon fitting of CUR release data to different mathematical models.

Kinetic model	pH	R^2	Kinetic characteristics
Zero-order	5.4	0.7841	K_0= 0.8620
Zero-order	7.4	0.8522	K_0= 0.5702
First-order	5.4	0.9952	K_1= 0.0336
First-order	7.4	0.9437	K_1= 0.0096
Higuchi	5.4	0.9656	K_H= 0.0993
Higuchi	7.4	0.9852	K_H= 0.0633
Korsmeyer-Peppas	5.4	0.9832	K= 0.1964, n = 0.36
Korsmeyer-Peppas	7.4	0.9864	K= 0.1117, n = 0.38
Hixson-Crowell	5.4	0.9539	K_{HC}= 0.0067
Hixson-Crowell	7.4	0.9179	K_{HC}= 0.0027
Weibull	5.4	0.9952	β= 0.0336, α= 8.31
Weibull	7.4	0.9437	β= 0.0096, α= 10.52
Baker	5.4	0.9970	K_{BL}= 0.0040
Baker	7.4	0.9907	K_{BL}= 0.0010

(~3 %), the nanocarrier showed a more consistent and prolonged cytotoxic effect. This is therapeutically relevant, as free CUR is known to degrade rapidly due to poor solubility and a short half-life under physiological conditions. In contrast, encapsulated CUR remained bioavailable for a longer duration, contributing to sustained cytotoxicity.

Moreover, the polymeric carriers alone (CS, CS/SA, and CS/SA/CeO_2) demonstrated viabilities above 88 % in astrocytes, confirming their biosafety. Overall, CS/SA/CeO_2@CUR exhibited selective cytotoxicity toward cancer cells, a key criterion in brain tumor therapy. The observed difference in cell viability exceeding 35 % (85 % vs. 50 %) between healthy and cancerous cells underscores the nanocarrier's targeting ability and therapeutic selectivity [72]. Although the viability of U-87MG2 glioma cells following treatment with CS/SA/CeO_2@CUR nanocarriers remained ca. 50 %, near that of free CUR, the therapeutic implications extend beyond. The viability reduction comparing blank nanocarriers (~ 90 %) and CUR-loaded ones (~50 %) represents a statistically significant ~ 40 % reduction (***$p < 0.0001$), confirming the potent cytotoxic effect of the encapsulated drug. Moreover, flow cytometry analysis (Fig. 7) revealed that the nanocarrier induced a higher rate of late apoptosis (67.4 %) compared to free CUR (58.5 %), indicating that the former cell death mechanism was more efficient and influenced by the nanocomposite (see below). This apoptotic pathway is clinically relevant, as it minimizes inflammation commonly associated with necrosis. In addition, the observed sustained cytotoxicity is consistent with the pH-responsive and prolonged release behavior of CUR from the nanocarrier (up to 96.5 % release at pH 5.4), ensuring enhanced bioavailability in tumor-like acidic environments. Furthermore, the inclusion of CeO_2 nanoparticles may support the prolonged therapeutic activity of CUR by contributing to its physicochemical stabilization. This effect is potentially associated with the inherent redox activity of CeO_2, which has been widely reported to modulate reactive oxygen species (ROS) levels in biological environments. This can be

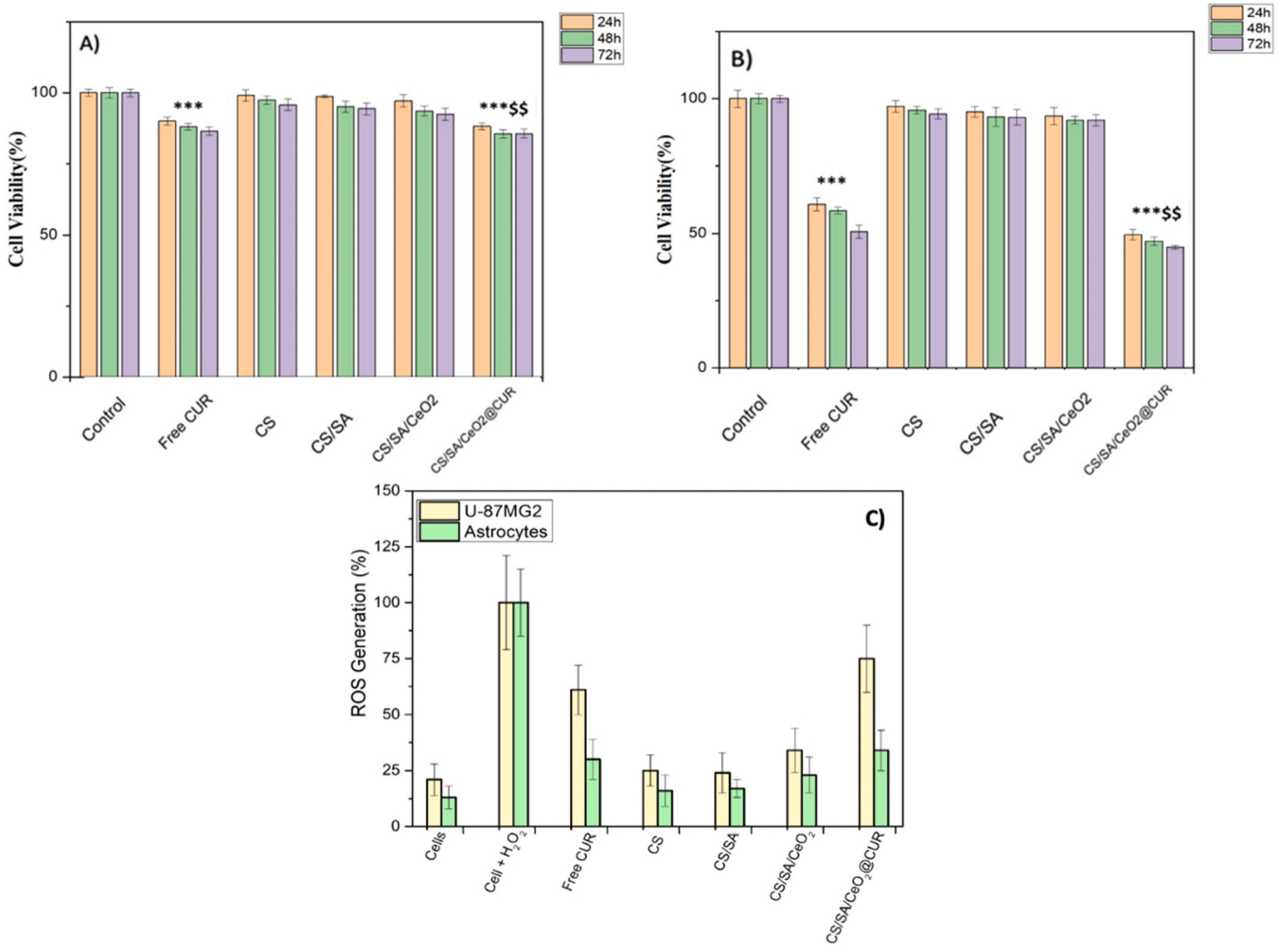

Fig. 6. Cytotoxicity of free CUR, CS, CS/SA, CS/SA/CeO_2, and CS/SA/CeO_2@CUR hybrid NPs in A) healthy astrocytes and B) (U-87MG2) glioma cells after 24, 48 and 72 h of treatment. C) ROS generation of free CUR, CS, CS/SA, CS/SA/CeO_2, and CS/SA/CeO_2@CUR hybrid NPs after 24 h. data are presented as mean ± SD (n = 3)).

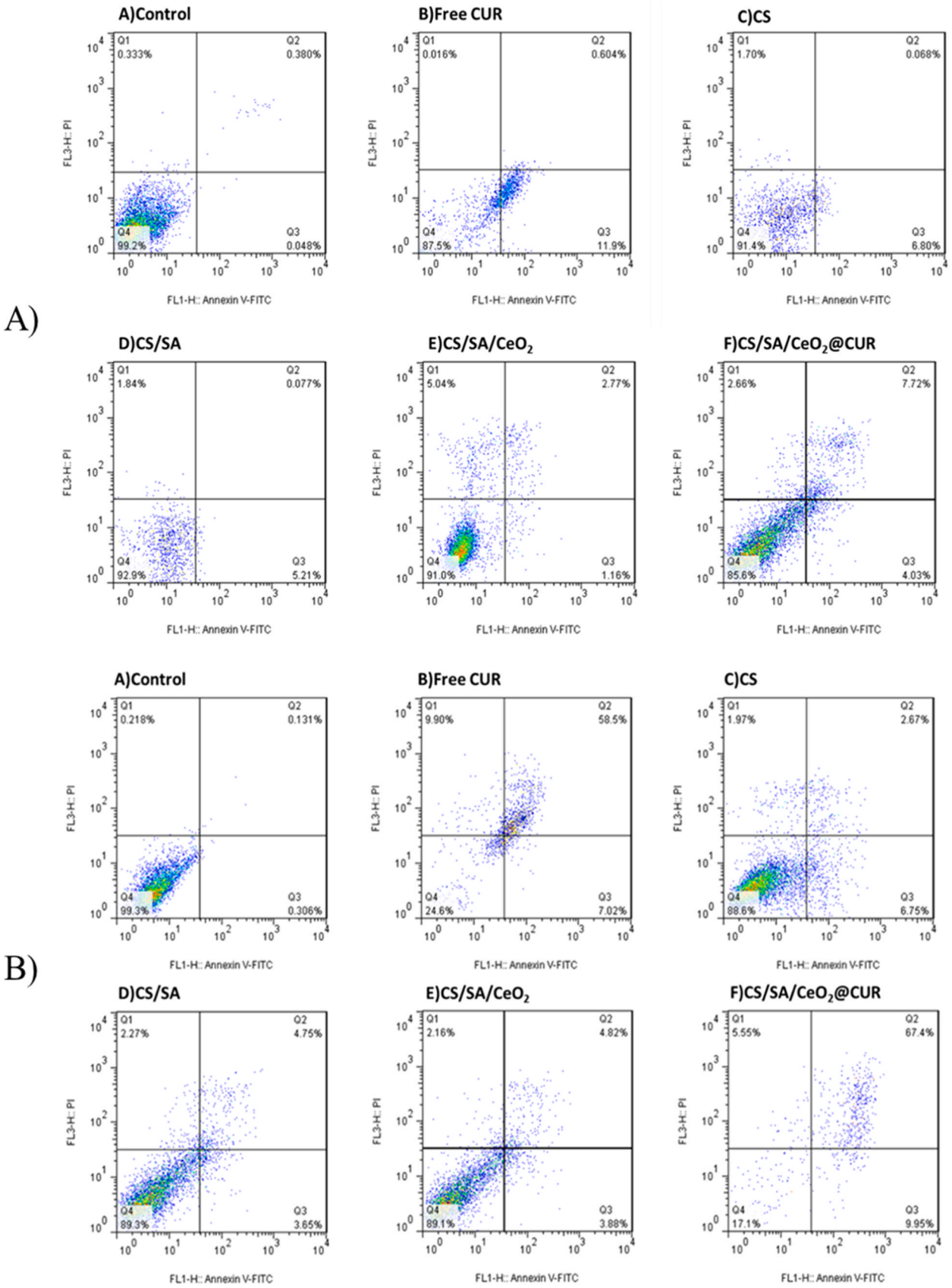

Fig. 7. Annexin V/PI staining for (A) astrocytes (normal cells) and (B) U87MG2 cells (cancer cells) treated with the control group (unstained cells), free CUR, CS, CS/SA, CS/SA/CeO_2, and CS/SA/CeO_2@CUR after 48 h of incubation obtained by flow cytometry. The bottom left quadrant Aannexin V-/PI-) indicates viable cells, the top left quadrant (Annexin V-/PI+) represents necrotic cells, the bottom right quadrant (Annexin V+/PI-) shows early apoptotic cells, and the top right quadrant (Annexin V+/PI+) displays late apoptotic cells.

observed in Fig. 6**C,** in which the combination of CeO_2 NPs with CUR inside the nanocarrier elevated the production of ROS compared to either the free drug or the inorganic NPs alone. In fact, it has been shown that CeO_2 NPs may protect sensitive drug molecules from premature degradation in oxidizing environments while potentially contributing to cell death thanks to ROS [22]. Taken together, these findings demonstrate that despite the modest numerical differences in cell viability, the CS/SA/CeO_2@CUR formulation offers mechanistically superior, sustained, and selective anti-tumor activity. Flow cytometry analysis was further performed to elucidate the underlying mechanism of cell death.

On the other hand, the cell death mechanisms promoted by CS/SA/CeO_2@CUR nanoparticles were assessed using the Annexin V-propidium iodide (PI) assay by flow cytometry on both astrocyte and U-87MG2 brain cell lines after 15 min of incubation at 4 °C in darkness. This assay is based on the detection of translocation of phosphatidylserine to the outer plasma membrane, indicating the onset of apoptosis or programmed cell death. Early apoptotic cells did not show detectable PI, a non-permeable dye, staining due to the integrity of the plasma membrane [21]; however, in the later stages of apoptosis and in cell necrosis, the plasma and nuclear membranes are compromised allowing the uptake of PI, which binds to DNA and emits red fluorescence [73]. Figs. 7A-B highlight the four quadrant zones Q1, Q2, Q3, and Q4, identifying necroptotic or necrotic cells as FITC-negative/PI-positive, cells in late apoptosis as FITC-positive/PI-positive, early apoptotic cells as FITC-positive/PI-negative, and healthy cells as FITC-negative/PI-negative [74].

For astrocyte cells (Fig. 7A), the flow cytometry data are in agreement with those of the MTT assay, confirming a very slight reduction of cell viability when CS, CS/SA, and CS/SA/CeO_2 are administered to cells. The percentages of viable cells in these groups were 91.4 %, 92.9 %, and 91.0 %, respectively, with late apoptosis and necrosis rates remaining below 5 %. The CS/SA/CeO_2@CUR-treated group exhibited a reduction in viable cells to 85.6 %, with 4.03 % of cells undergoing early apoptosis, 7.72 % in late apoptosis, and 2.66 % in necrosis. These values were slightly elevated compared to free CUR (viable: 98.5 %; early apoptosis: 0.081 %; late apoptosis: 0.604 %; necrosis: 0.016 %), indicating that the carrier maintains acceptable safety while delivering the drug. This finding, consistent with data in Fig. 6A, highlights the carrier's efficacy in delivering the therapeutic agent to normal cells with minimal adverse effects.

On the other hand, flow cytometry data for U-87MG2 cells (Fig. 7B) confirmed viability rates of 88.6 %, 89.3 %, and 89.1 % for the CS, CS/SA, and CS/SA/CeO_2-treated groups, respectively, again supporting their biocompatibility. In contrast, free CUR treatment reduced viability to 24.4 %, with 7.26 % early and 58.5 % late apoptotic cells, while the CS/SA/CeO_2@CUR-treated group showed the highest apoptotic response, with only 17.0 % viable cells and elevated rates of early (10.0 %) and late (67.4 %) apoptosis, along with 5.55 % necrosis. These results indicate that the incorporation of CeO_2 and CUR within the nanocarrier enhances pro-apoptotic efficacy against glioma cells [75]. These flow cytometry results further validate the findings of the MTT assay (Fig. 6B), where CS/SA/CeO_2@CUR exhibited sustained tumor cell suppression over 72 h. The enhanced apoptotic profile observed here confirms that, despite the similar final viability values compared to free CUR, the nanocarrier promotes a more effective and regulated cell death mechanism, which is critical for long-term therapeutic success and tumor inhibition.

Conversely, the hybrid CS/SA/CeO_2@CUR NPs (Fig. 7B) containing the drug showed early and late cell apoptosis rates of ca. 10 % and 67.4 %, which are higher than those observed when free CUR is administered to cells (7.0 % and 58.5 %). This enhancement in apoptosis can be attributed to the combination of CUR and CeO_2 NPs within the nanocarrier. The sustained release of the drug ensures prolonged intracellular bioavailability. Simultaneously, the inherent oxidase activity of CeO_2 at acidic pH—mimicking tumor microenvironments—may modulate oxidative stress and enhance the therapeutic bioactivity of CUR [76]. CeO_2 NPs possess a unique redox-switching capability arising from reversible transitions between Ce^{3+} and Ce^{4+} oxidation states, mediated by oxygen vacancies on their surface [76]. This dual redox function enables, for example, CeO_2 to selectively promote oxidative stress in cancer cells while protecting healthy neural tissues [77]. At this respect, it has been shown that CUR rapidly degrades in solution in an autoxidation reaction enhanced by oxidizing agents, such as dissolved oxygen, with the formation of various chemical species [77]. As CeO_2 NPs might also act simultaneously as ROS scavengers in a dynamic balance, it seems that they would influence the CUR oxidation process significantly reducing its degradation rate in aqueous solutions in agreement with previous reports, thus enhancing the therapeutic activity of the drug and sustaining its pro-apoptotic activity [78]. Moreover, the dual redox function enables CeO_2 to selectively promote oxidative stress in cancer cells while protecting healthy neural tissues [79], in contrast to other redox-active nanomaterials as, for example, MnO_2 NPs which act primarily by depleting intracellular glutathione (GSH) and generating Mn^{2+}; however, their function is highly dependent on elevated GSH levels and can result in neurotoxicity in non-targeted tissues [80]. Fe_3O_4 NPs generate hydroxyl radicals via Fenton-like reactions but often lack redox specificity and may cause nonspecific oxidative damage [81]. On the other hand TiO_2 NPs, although effective for photodynamic applications, requires external UV activation, limiting its activity in deep tissues such as the brain [82]. In contrast, CeO_2 NPs offer endogenous, stimulus-free ROS modulation, with the ability to toggle between protective and pro-oxidant effects depending on the microenvironment [83].

In summary, these findings confirm that the redox-responsive CeO_2-based nanocarrier system not only enhances apoptotic signaling in glioma cells—as evidenced by the significantly higher rate of late apoptosis in CS/SA/CeO_2@CUR-treated cells (67.4 %) compared to free CUR (58.5 %)—but also stabilizes curcumin, ultimately contributing to a more sustained and targeted anticancer response suitable for brain tumor therapy.

4. Conclusions

CUR holds great promise as an anticancer agent, but its clinical application is limited by inherent drawbacks, such as its poor solubility and a short biological half-life, which complicate sustained and targeted delivery. To address these challenges, a pH-responsive nanocarrier, CS/SA/CeO_2/CUR, was developed using a water-in-oil-in-water (W/O/W) emulsification technique. Comprehensive physicochemical analyses, including FE-SEM, XRD and FTIR, validated the successful synthesis and characterization of the developed nanocarrier. In this manner, DLS and zeta potential analysis showed an average particle size of 170 nm and a favorable surface charge of + 119.32 mV, while FE-SEM imaging revealed nanoparticles with irregular spherical shapes and textured surfaces. The loading efficiency (LE%) and encapsulation efficiency (EE %) of CUR inside the carrier were 49 % and 86 %, respectively. *In vitro* drug release studies at pH 5.4 and 7.4 demonstrated the pH-responsive nature of the nanocarrier. After 96 h, 96.5 % of CUR was released under acidic conditions compared to 64 % in physiological ones, with the release kinetics controlled by a diffusion-driven process regulated by the nanocarrier swelling as denoted by the Baker-Lonsdale model.

Cytotoxicity evaluations using the MTT assay revealed minimal cytotoxicity in CS, CS/SA and CS/SA-CeO_2-treated cell groups compared to the control group (untreated cells). Importantly, the CUR-loaded CS/SA/CeO_2 hybrid NPs significantly outperformed free CUR in reducing cancer cell viability, which was demonstrated to be specific to glioma cells. Flow cytometry findings further validated these results, revealing distinct cell death mechanisms in both astrocyte and U-87MG2 glioma cells. For astrocytes, CS/SA/CeO_2@CUR exhibited a slight reduction in viable cells (85.6 %) compared to the control group (99.2 %), with early apoptosis accounting for 7.72 % and late apoptosis for 4.03 %. Conversely, in U-87MG2 glioma cells, CS/SA/CeO_2@CUR significantly

increased late apoptosis (67.4 %) compared to free CUR (58.5 %), highlighting the potential protective role of ROS scavenger of the inorganic NPs in preventing early drug oxidation and subsequent degradation in solution. These findings underscore the enhanced therapeutic potential of hybrid CS/SA/CeO_2@CUR NPs in selectively inducing targeted apoptosis in brain tumoral cells, positioning them as a promising candidate for anticancer treatment.

CRediT authorship contribution statement

Pablo Taboada: Writing – review & editing, Validation. **Salar Mohammadi Shabestari:** Writing – original draft, Visualization, Validation, Software, Investigation, Formal analysis, Data curation, Conceptualization. **Mehrab Pourmadadi:** Writing – review & editing, Visualization, Validation. **Hamidreza Abdouss:** Writing – review & editing, Visualization, Validation. **Taranom Ghanbari:** Resources. **Majid Abdouss:** Writing – review & editing, Visualization, Validation, Supervision. **Abbas Rahdar:** Writing – review & editing. **Adriana Cambón:** Validation, Software, Investigation, Data curation.

Declaration of Competing Interest

The authors declare that they have no known competing financial interests or personal relationships that could have appeared to influence the work reported in this paper.

Acknowledgements

P.T thanks Agencia Estatal de Investigación (AEI) for funding through project PID2022–142682OB-I00 and PCI2022–134981–2, and Xunta de Galicia for grant ED431C 2022/28. ERDF funds are also acknowledged.

Data availability

Data will be made available on request.

References

[1] Y. Zhao, P. Yue, Y. Peng, Y. Sun, X. Chen, Z. Zhao, B. Han, Recent advances in drug delivery systems for targeting brain tumors, Drug Deliv. 30 (2023) 1–18, https://doi.org/10.1080/10717544.2022.2154409.
[2] H. Sung, J. Ferlay, R.L. Siegel, M. Laversanne, I. Soerjomataram, A. Jemal, F. Bray, Global cancer statistics 2020: GLOBOCAN estimates of incidence and mortality worldwide for 36 cancers in 185 countries, Cancer J. Clin. 71 (2021) 209–249, https://doi.org/10.3322/caac.21660.
[3] G. Reifenberger, H.-G. Wirsching, C.B. Knobbe-Thomsen, M. Weller, Advances in the molecular genetics of gliomas — implications for classification and therapy, Nat. Rev. Clin. Oncol. 14 (2017) 434–452, https://doi.org/10.1038/nrclinonc.2016.204.
[4] T.T.T. Nguyen, L.A. Greene, H. Mnatsakanyan, C.E. Badr, Revolutionizing brain tumor care: emerging technologies and strategies, Biomedicines 12 (2024) 1376, https://doi.org/10.3390/biomedicines12061376.
[5] P. Salahshour, Nanobiomaterials/bioinks based scaffolds in 3d bioprinting for tissue engineering and artificial human organs, Adv. Biol. Earth Sci. 9 (2024) 97–104, https://doi.org/10.62476/abes9s97.
[6] A. Nasibova, The modern perspectives of nanomaterial applications in cancer treatment and drug delivery, Adv. Biol. Earth Sci. 9 (2024) 330–337, https://doi.org/10.62476/abes93330.
[7] Z. Qiu, Z. Yu, T. Xu, L. Wang, N. Meng, H. Jin, B. Xu, Novel nano-drug delivery system for brain tumor treatment, Cells 11 (2022) 3761, https://doi.org/10.3390/cells11233761.
[8] S.M. Shabestari, S.H. Jafari, S.Z. Benisi, R. Khoeini, S. Shojaei, M. Ghorbani, V. Goodarzi, Role of phosphate-modified cellulose into the scaffold based on poly (glycerol azelaic acid)-co-poly(ε-caprolactone) for using bone regenerative Medicine, Int. J. Biol. Macromol. 304 (2025) 140855, https://doi.org/10.1016/j.ijbiomac.2025.140855.
[9] A. Unnisa, N.H. Greig, M.A. Kamal, Nanotechnology: a promising targeted drug delivery system for brain tumours and Alzheimer's disease, Curr. Med. Chem.. 30 (2023) 255–270, https://doi.org/10.2174/0929867329666220328125206.
[10] T.C. Ezike, U.S. Okpala, U.L. Onoja, C.P. Nwike, E.C. Ezeako, O.J. Okpara, C. C. Okoroafor, S.C. Eze, O.L. Kalu, E.C. Odoh, U.G. Nwadike, J.O. Ogbodo, B. U. Umeh, E.C. Ossai, B.C. Nwanguma, Advances in drug delivery systems, challenges and future directions, Heliyon 9 (2023) e17488, https://doi.org/10.1016/j.heliyon.2023.e17488.
[11] M.Y. Leong, Y.L. Kong, K. Burgess, W.F. Wong, G. Sethi, C.Y. Looi, Recent development of nanomaterials for transdermal drug delivery, Biomedicines 11 (2023) 1124, https://doi.org/10.3390/biomedicines11041124.
[12] C.O. Egwu, C. Aloke, K.T. Onwe, C.I. Umoke, J. Nwafor, R.A. Eyo, J.A. Chukwu, G. O. Ufebe, J. Ladokun, D.T. Audu, A.O. Agwu, D.C. Obasi, C.O. Okoro, Nanomaterials in drug delivery: strengths and opportunities in Medicine, Molecules 29 (2024) 2584, https://doi.org/10.3390/molecules29112584.
[13] L. Yang, M. Yuan, P. Ma, X. Chen, Z. Cheng, J. Lin, Assembling AgAuSe quantum dots with peptidoglycan and neutrophils to realize enhanced tumor targeting, NIR (II) imaging, and sonodynamic therapy, Small Methods 7 (2023) e2201706, https://doi.org/10.1002/smtd.202201706.
[14] J.K. Patra, G. Das, L.F. Fraceto, E.V. Ramos-Campos, M.P. Rodríguez-Torres, L. S. Acosta-Torres, L.A. Díaz-Torres, R. Grillo, M.K. Swamy, S. Sharma, S. Habtemariam, H.-S. Shin, Nano based drug delivery systems: recent developments and future prospects, J. Nanobiotechnol. 16 (2018) 1–33, https://doi.org/10.1186/s12951-018-0392-8, 2018.
[15] S.M. Shabestari, M. Pourmadadi, H. Abdouss, T. Ghanbari, S. Bazari, M. Abdouss, A. Rahdar, L.F. Romanholo-Ferreira, Unlocking the potential of cytarabine: a comprehensive review from molecular insights to advanced nanoformulations and co-delivery strategies for enhanced drug efficacy, J. Drug Deliv. Sci. Technol. 102 (2024) 106346, https://doi.org/10.1016/j.jddst.2024.106346.
[16] E. Yeini, P. Ofek, N. Albeck, D. Rodríguez-Ajamil, L. Neufeld, A. Eldar-Boock, R. Kleiner, D. Vaskovich, S. Koshrovski-Michael, S.I. Dangoor, A. Krivitsky, C. Burgos-Luna, G. Shenbach-Koltin, M. Goldenfeld, O. Hadad, G. Tiram, R. Satchi-Fainaro, Targeting glioblastoma: advances in drug delivery and novel therapeutic approaches, Adv. Ther. 4 (2021) 2000124, https://doi.org/10.1002/adtp.202000124.
[17] P.-C. Peng, R.-L. Hong, T. Tsai, C.-T. Chen, Co-encapsulation of chlorin e6 and chemotherapeutic drugs in a PEGylated liposome enhance the efficacy of tumor treatment: pharmacokinetics and therapeutic efficacy, Pharmaceutics 11 (2019) 617, https://doi.org/10.3390/pharmaceutics11110617.
[18] R. Khalilov, Interactions of nanoparticles and biological systems, Adv. Biol. Earth Sci. 9 (2024) 311–318, https://doi.org/10.62476/abes93311.
[19] V. Kailasam, S.S. Cheruvu, M. Malani, S.M. Sai Kameswari, P. Kesharwani, J. Nirmal, Recent advances in novel formulation approaches for tacrolimus delivery in treatment of various ocular diseases, J. Drug Deliv. Sci. Technol. 78 (2022) 103945, https://doi.org/10.1016/j.jddst.2022.103945.
[20] Z. Feyisa, N.K. Gupta, G.D. Edossa, A. Sundaramurthy, A. Kapoor, L.G. Inki, Fabrication of pH-sensitive double cross-linked sodium alginate/chitosan hydrogels for controlled release of amoxicillin, Polym. Eng. Sci. 63 (2023) 2546–2564, https://doi.org/10.1002/pen.26395.
[21] H. Abdouss, M. Pourmadadi, P. Zahedi, M. Abdouss, Green synthesis of chitosan /polyacrylic acid /graphitic carbon nitride nanocarrier as a potential pH-sensitive system for curcumin delivery to MCF-7 breast cancer cells, Int. J. Biol. Macromol. 242 (2023) 125134, https://doi.org/10.1016/j.ijbiomac.2023.125134.
[22] Y.-C. Lin, Y.-J. Liang, C.-H. Zhang, L.-J. Liu, F.-H. Lin, Characterization and therapeutic potential of curcumin-loaded cerium oxide nanoparticles for interstitial cystitis management, Antioxidants 13 (2024) 826, https://doi.org/10.3390/antiox13070826.
[23] R. Wang, D. Shou, O. Lv, Y. Kong, L. Deng, J. Shen, pH-Controlled drug delivery with hybrid aerogel of chitosan, carboxymethyl cellulose and graphene oxide as the carrier, Int. J. Biol. Macromol. 103 (2017) 248–253, https://doi.org/10.1016/j.ijbiomac.2017.05.064.
[24] M. Olukman Şahin, O. Şanlı, In vitro 5-fluorouracil release properties investigation from ph sensitive sodium alginate coated and uncoated methyl cellulose/chitosan microspheres, Int. J. Biol. Macromol. 258 (2024) 128895, https://doi.org/10.1016/j.ijbiomac.2023.128895.
[25] O.D. Frent, L.G. Vicas, N. Duteanu, C.M. Morgovan, T. Jurca, A. Pallag, M. E. Muresan, S.M. Filip, R.-L. Lucaciu, E. Marin, Sodium alginate—Natural microencapsulation material of polymeric microparticles, Int. J. Mol. Sci. 23 (2022) 12108, https://doi.org/10.3390/ijms232012108.
[26] K. Kalantari, E. Mostafavi, B. Saleh, P. Soltantabar, T.J. Webster, Chitosan/PVA hydrogels incorporated with Green synthesized cerium oxide nanoparticles for wound healing applications, Eur. Polym. J. 134 (2020) 109853, https://doi.org/10.1016/j.eurpolymj.2020.109853.
[27] A. Mari, M.V. Vincent, D. Pachiyappan, R. Mookkaiah, U. Sambath, Structural, optical and photocatalytic properties of cerium oxide nanoparticles, Nanochemistry Res. 10 (8) (2025) 1, https://doi.org/10.22036/ncr.2025.01.001.
[28] A.G. Niculescu, A.M. Grumezescu, Applications of chitosan-alginate-based nanoparticles— an up-to-date review, Nanomaterials 12 (2022) 186, https://doi.org/10.3390/nano12020186.
[29] M. Pourmadadi, S.M. Shabestari, H. Abdouss, Z. Amiri, M. Abdouss, A. Rahdar, S. Padey, Green synthesis of pH-sensitive carboxymethyl cellulose/agarose/carbon quantum dots nanocarriers for quercetin delivery to A549 lung cancer using an emulsification method, Bionanoscience 14 (2024) 4570–4584, https://doi.org/10.1007/s12668-024-01426-9.
[30] N. Jackson, A.C. Ortiz, A. Jerez, J. Morales, F. Arriagada, Kinetics and mechanism of camptothecin release from transferrin-gated mesoporous silica nanoparticles through a pH-responsive surface linker, Pharmaceutics 15 (2023) 1590, https://doi.org/10.3390/pharmaceutics15061590/S1.
[31] S.A. Ganie, R.A. Naik, O.A. Dar, L.J. Rather, M.A. Assiri, Q. Li, Design and fabrication of functionalized curdlan-curcumin delivery system to facilitate the therapeutic effects of curcumin on breast cancer, Int. J. Biol. Macromol. 267 (2024) 131388, https://doi.org/10.1016/j.ijbiomac.2024.131388.

[32] J. Xue, Y. Luo, Protein-polysaccharide nanocomplexes as nanocarriers for delivery of curcumin: a comprehensive review on preparation methods and encapsulation mechanisms, J. Futur. Foods 3 (2023) 99–114, https://doi.org/10.1016/j.jfutfo.2022.12.002.
[33] J. Wang, Y. Ma, Q. Meng, Y. Yang, R. Zhang, S. Zhong, Y. Gao, W. He, X. Cui, Photocrosslinked carboxymethylcellulose-based hydrogels: synthesis, characterization for curcumin delivery and wound healing, Int. J. Biol. Macromol. 275 (2024) 133558, https://doi.org/10.1016/j.ijbiomac.2024.133558.
[34] S. Pan-On, P. Dilokthornsakul, W. Tiyaboonchai, Trends in advanced oral drug delivery system for curcumin: a systematic review, J. Control. Release 348 (2022) 335–345, https://doi.org/10.1016/j.jconrel.2022.05.048.
[35] Y. Xia, R. Xu, S. Ye, J. Yan, P. Kumar, P. Zhang, Z. Zhao, Microfluidic formulation of curcumin-loaded multiresponsive gelatin nanoparticles for anticancer therapy, ACS Biomater. Sci. Eng. 9 (2023) 3402–3413, https://doi.org/10.1021/acsbiomaterials.3c00318.
[36] P.R. Ravi, U.K. Kotreka, R.N. Saha, Controlled release matrix tablets of zidovudine: effect of formulation variables on the in vitro drug release kinetics, AAPS PharmSciTech 9 (2008) 302–313, https://doi.org/10.1208/s12249-007-9030-8.
[37] F. Mohajjel, M. Pourmadadi, M. Abdouss, Synthesis and performance evaluation of a nanocomposite comprising polyacrylamide hydrogel reinforced with pectin and titanium dioxide for the delivery of curcumin, Carbohydr. Polym. Technol. Appl. 10 (2025) 100854, https://doi.org/10.1016/j.carpta.2025.100854.
[38] M. Pooresmaeil, H. Namazi, Facile preparation of pH-sensitive chitosan microspheres for delivery of curcumin; characterization, drug release kinetics and evaluation of anticancer activity, Int. J. Biol. Macromol. 162 (2020) 501–511, https://doi.org/10.1016/j.ijbiomac.2020.06.183.
[39] N. Lakshani, H.S. Wijerathne, C. Sandaruwan, N. Kottegoda, V. Karunarathne, Release kinetic models and release mechanisms of controlled-release and slow-release fertilizers, ACS Agric. Sci. Technol. 3 (2023) 939–956, https://doi.org/10.1021/acsagscitech.3c00152.
[40] R. Khoz, M. Pourmadadi, F. Yazdian, A. Rhadar, S. Razzaq, S. Fathi-Karkan, M. A. Aboudzadeh, Quercetin-loaded gelatin/agarose/Fe_2O_3 hybrid nanocarriers in a microemulsion matrix: synthesis, characterization, and cancer therapeutic potential, Mater. Today Commun. 46 (2025) 112597, https://doi.org/10.1016/j.mtcomm.2025.112597.
[41] N.S. Heredia, K. Vizuete, M. Flores-Calero, K. Pazmiño V, F. Pilaquinga, B. Kumar, A. Debut, Comparative statistical analysis of the release kinetics models for nanoprecipitated drug delivery systems based on poly(lactic-co-glycolic acid), PLoS One 17 (2022) e0264825, https://doi.org/10.1371/journal.pone.0264825.
[42] A.M. Asl, M. Abdouss, M.R. Kalaee, S.S. Homami, M. Pourmadadi, Targeted delivery of quercetin using gelatin/starch/Fe_3O_4 nanocarrier to suppress the growth of liver cancer HepG2 cells, Int. J. Biol. Macromol. 281 (2024) 136535, https://doi.org/10.1016/j.ijbiomac.2024.136535.
[43] U.de J. Martín-Camacho, N. Rodríguez-Barajas, J.A. Sánchez-Burgos, A. Pérez-Larios, Weibull β value for the discernment of drug release mechanism of PLGA particles, Int. J. Pharm.. 640 (2023) 123017, https://doi.org/10.1016/j.ijpharm.2023.123017.
[44] C. Corsaro, G. Neri, A.M. Mezzasalma, E. Fazio, Weibull modeling of controlled drug release from Ag-PMA nanosystems, Polym. (Basel) 13 (2021) 2897, https://doi.org/10.3390/polym13172897.
[45] M. Danaei, M. Dehghankhold, S. Ataei, F.H. Davarani, R. Javanmard, A. Dokhani, S. Khorasani, M.R. Mozafari, Impact of particle size and polydispersity index on the clinical applications of lipidic nanocarrier systems, Pharmaceutics 18 (2018) 57, https://doi.org/10.3390/pharmaceutics10020057.
[46] K. Khezri, M. Saeedi, H. Mohammadamini, A.S. Zakaryaei, A comprehensive review of the therapeutic potential of curcumin nanoformulations, Phyther. Res. 35 (2021) 5527–5563, https://doi.org/10.1002/ptr.7190.
[47] P. Dong, K.P. Rakeh, H.M. Manukumar, Y.H.E. Mohammed, C.S. Karthik, S. Sumathi, P. Mallu, H.-L. Qin, Innovative nano-carriers in anticancer drug delivery-a comprehensive review, Bioorg. Chem. 85 (2019) 325–336, https://doi.org/10.1016/j.bioorg.2019.01.019.
[48] P. Sharma, V. Jain, M. Tailang, Advancement of nanocarrier-based engineering for specific drug delivery for cancer therapy. Targeted Cancer Therapy in Biomedical Engineering, Springer, Singapore, 2023, pp. 465–486, 10.1007/978-981-19-9786-0_13.
[49] E. Joseph, G. Singhvi, Multifunctional nanocrystals for cancer therapy: a potential nanocarrier. Nanomaterials for Drug Delivery and Therapy, Elsevier, 2019, pp. 91–116, 10.1016/B978-0-12-816505-8.00007-2.
[50] R. Shah, D. Eldridge, E. Palombo, I. Harding, Optimisation and stability assessment of solid lipid nanoparticles using particle size and zeta potential, J. Phys. Sci. 25 (2014) 59–75, 2014.
[51] M. Pourmadadi, S. Darvishan, M. Abdouss, F. Yazdian, A. Rahdar, A.M. Díez-Pascual, pH-responsive polyacrylic acid (PAA)-carboxymethyl cellulose (CMC) hydrogel incorporating halloysite nanotubes (HNT) for controlled curcumin delivery, Ind. Crops Prod. 197 (2023) 116654, https://doi.org/10.1016/j.indcrop.2023.116654.
[52] A. Samadi, S. Haseli, M. Pourmadadi, H. Rashedi, F. Yazdian, M. Navaei-Nigjeh, Curcumin-loaded chitosan-agarose-montmorillonite hydrogel nanocomposite for the treatment of breast cancer, in 2020 27th national and 5th international Iranian conference on biomedical engineering (ICBME), IEEE, 2020, pp. 148–153, 10.1109/ICBME51989.2020.9319425.
[53] K. Baysal, A.Z. Aroguz, Z. Adiguzel, B.M. Baysal, Chitosan/alginate crosslinked hydrogels: preparation, characterization and application for cell growth purposes, Int. J. Biol. Macromol. 59 (2013) 342–348, https://doi.org/10.1016/j.ijbiomac.2013.04.073.
[54] A. Hasan, G. Waibhaw, S. Tiwari, K. Dharmalingam, I. Shukla, L.M. Pandey, Fabrication and characterization of chitosan, polyvinylpyrrolidone, and cellulose nanowhiskers nanocomposite films for wound healing drug delivery application, J. Biomed. Mater. Res. Part A 105 (2017) 2391–2404, https://doi.org/10.1002/jbm.a.36097.
[55] S. Bhatia, A. Al-harrasi, M.S. Al-Azri, S. Ullah, A.E.-D.A. Bekhit, A. Pratap-Singh, M. K. Chatli, K. anwer, M.F. Aldawsari, Preparation and physiochemical characterization of bitter Orange oil loaded sodium alginate and casein based edible films, Polym. (Basel) 14 (2022) 3855, https://doi.org/10.3390/polym14183855.
[56] A.F. Hassan, H.M.A. Salam, F. Mohamed, O.F. Abdel-Gawad, The optimization performance of fibrous sodium alginate co-polymer in direct methanol/ethanol fuel cells, J. Polym. Environ. 31 (2023) 3664–3676, https://doi.org/10.1007/s10924-023-02852-8.
[57] A. Suratman, A.D. Oktaviani, N.H. Aprilita, A.H. Wibowo, Alginate-chitosan hydrogel as controlled release of NPK macronutrient, IOP Conf. Ser. Mater. Sci. Eng. 578 (2019) 012074, https://doi.org/10.1088/1757-899X/578/1/012074.
[58] M.T. ALSamman, J. Sánchez, Adsorption of copper and arsenic from water using a semi-interpenetrating polymer network based on alginate and chitosan, Polymers 15 (2023) 2192, https://doi.org/10.3390/polym15092192.
[59] A.L. Khan, Dhanjai, R. Jain, Fabrication and optimization of polypyrrole/cerium oxide/glassy carbon sensing platform for the electrochemical detection of flupirtine, J. Appl. Electrochem.. 50 (2020) 655–672, https://doi.org/10.1007/s10800-020-01418-z.
[60] G. Wang, X. Wang, L. Huang, Feasibility of chitosan-alginate (Chi-Alg) hydrogel used as scaffold for neural tissue engineering: a pilot study in vitro, Biotechnol. Biotechnol. Equip. 31 (2017) 1–8, https://doi.org/10.1080/13102818.2017.1332493.
[61] A.C.R. Gonçalves, L.G.R. Duarte, A.C.T.R. Fiocco, W.M.P. Alencar, R. Iacuzio, N.C. C. Silva, C.S.F. Picone, Improving chitosan properties through ionic and chemical cross-linking and their impact on emulsified systems, Int. J. Food Sci. Technol. 58 (2023) 4324–4331, https://doi.org/10.1111/ijfs.16533.
[62] M.K. Mohanapriya, K. Deshmukh, M.B. Ahamed, K. Chidambaram, S.K. Khadheer Pasha, Influence of cerium oxide (CeO_2) nanoparticles on the structural, morphological, mechanical and dielectric properties of PVA/PPy blend nanocomposites, Mater. Today Proc. 3 (2016) 1864–1873, https://doi.org/10.1016/j.matpr.2016.04.086.
[63] D. Kumarasamy, T.K. Giri, Biopolysaccharide-based hydrogel materials for drug delivery. Polysaccharide Carriers for Drug Delivery, Elsevier, 2019, pp. 585–613, 10.1016/B978-0-08-102553-6.00020-9.
[64] D. Hernandez-Patlan, B. Solis-Cruz, M.A. Cano-Vega, E. Beyssac, G. Garrait, X. Hernández-Velasco, R. López-Arellano, G. Téllez, G. R. Rivera-Rodríguez, development of chitosan and alginate nanocapsules to increase the solubility, permeability and stability of curcumin, J. Pharm. Innov. 14 (2019) 132–140, https://doi.org/10.1007/s12247-018-9341-1.
[65] Z. Lin, L. Zhan, K. Qin, Y. Li, Y. Qin, L. Yang, Q. Sun, N. Ji, F. Xie, Design and characterization of a novel core–shell nano delivery system based on zein and carboxymethylated short-chain amylose for encapsulation of curcumin, Foods 13 (2024) 1837, https://doi.org/10.3390/foods13121837.
[66] Z. Roshan, V. Haddadi-Asl, H. Ahmadi, M. Moussaei, Curcumin-encapsulated poly (lactic- co -glycolic acid) nanoparticles: a comparison of drug release kinetics from particles prepared via electrospray and nanoprecipitation, Macromol. Mater. Eng.. 309 (2024) 1–12, https://doi.org/10.1002/mame.202400040.
[67] C. Shen, J. Wang, X. Wu, J. Xu, J. Hu, A. Reheman, Drug release behavior of poly (amino acid)s drug-loaded nanoparticles with pH-responsive behavior, J. Drug Deliv. Sci. Technol. 87 (2023) 104827, https://doi.org/10.1016/j.jddst.2023.104827.
[68] M. Čierna, P. Mučaji, M. Špaglová, M. Čuchorová, O. Macho, Chitosan and sodium alginate implementation as pharmaceutical excipients in multiple-unit particulate systems, Polym. (Basel) 14 (2022) 2822, https://doi.org/10.3390/polym14142822.
[69] M. Yadav, B. Kaushik, G.K. Rao, C.M. Srivastava, D. Vaya, Advances and challenges in the use of chitosan and its derivatives in biomedical fields: a review, Carbohydr. Polym. Technol. Appl. 5 (2023) 100323, https://doi.org/10.1016/j.carpta.2023.100323.
[70] M. Dellali, C.E. Iurciuc (Tincu), C.L. Savin, N. Spahis, M. Djennad, M. Popa, Hydrogel films based on chitosan and oxidized carboxymethylcellulose optimized for the controlled release of curcumin with applications in treating dermatological conditions, Molecules 26 (2021) 2185, https://doi.org/10.3390/molecules26082185.
[71] Mathematical models of drug release. Strategies to Modify the Drug Release from Pharmaceutical Systems, Elsevier, 2015, pp. 63–86, 10.1016/B978-0-08-100092-2.00005-9.
[72] P. Kumar, A. Nagarajan, P.D. Uchil, Analysis of cell viability by the MTT assay, Cold Spring Harb. Protoc. (2018), https://doi.org/10.1101/pdb.prot095505.
[73] A.M. Rieger, K.L. Nelson, J.D. Konowalchuk, D.R. Barreda, Modified annexin v/propidium iodide apoptosis assay for accurate assessment of cell death, J. Vis. Exp. (50) (2011) 2–5, https://doi.org/10.3791/2597.
[74] M. Ramezani Farani, P. Khadiv-Parsi, G.H. Riazi, M. Shafiee Ardestani, H. Saligheh Rad, PEGylation of graphene/iron oxide nanocomposite: assessment of release of doxorubicin, magnetically targeted drug delivery and photothermal therapy, Appl. Nanosci. 10 (2020) 1205–1217, https://doi.org/10.1007/s13204-020-01255-8.
[75] M.S. Wason, J. Colon, S. Das, S. Seal, J. Turkson, J. Zhao, C.H. Baker, Sensitization of pancreatic cancer cells to radiation by cerium oxide nanoparticle-induced ROS production, Nanomed. Nanotechnol. Biol. Med. 9 (2013) 558–569, https://doi.org/10.1016/j.nano.2012.10.010, 76.

[76] A. Asati, S. Santra, C. Kaittanis, S. Nath, J.M. Perez, Oxidase-Like activity of Polymer-Coated cerium oxide nanoparticles, Angew. Chem. Int. Ed. 48 (2009) 2308–2312, https://doi.org/10.1002/anie.200805279, 77.
[77] C. Schneider, O.N. Gordon, R.L. Edwards, P.B. Luis, Degradation of curcumin: from mechanism to biological implications, J. Agric. Food Chem. 63 (2015) 7606–7614, https://doi.org/10.1021/acs.jafc.5b00244.78.
[78] N.M. Zholobak, A.B. Shcherbakov, O.S. Ivanova, V. Reukov, A.E. Baranchikov, V. K. Ivanov, Nanoceria-curcumin conjugate: synthesis and selective cytotoxicity against cancer cells under oxidative stress conditions, J. Photochem. Photobiol. B Biol. 209 (2020) 111921, https://doi.org/10.1016/j.jphotobiol.2020.111921.79.
[79] Y. Gao, X. Chen, H. Liu, A facile approach for synthesis of nano-CeO2 particles loaded co-polymer matrix and their colossal role for blood-brain barrier permeability in cerebral ischemia, J. Photochem. Photobiol. B Biol. 187 (2018) 184–189, https://doi.org/10.1016/j.jphotobiol.2018.05.003.
[80] M.H. Cho, E.S. Choi, S. Kim, S.H. Goh, Y. Choi, Redox-responsive manganese dioxide nanoparticles for enhanced MR imaging and radiotherapy of lung cancer, Front. Chem. 5 (2017) 1–10, https://doi.org/10.3389/fchem.2017.00109.
[81] W.K. Ong, X. Yao, D. Jana, M. Li, Y. Zhao, Z. Luo, Efficient production of reactive oxygen species from fe3o4/znpc coloaded nanoreactor for cancer therapeutics in vivo, Small Struct. 1 (2020) 2000065, https://doi.org/10.1002/sstr.202000065.
[82] S. Sargazi, S. Er, S.S. Gelen, A. rahdar, M. Bilal, R. Arshad, N. Ajalli, M.F.A. Khan, S. Pandey, Application of titanium dioxide nanoparticles in photothermal and photodynamic therapy of cancer: an updated and comprehensive review, J. Drug Deliv. Sci. Technol. 75 (2022) 103605, https://doi.org/10.1016/j.jddst.2022.103605.
[83] Z. Serebrovska, R.J. Swanson, V. Partnichenko, A. Shysh, S. Pavlovich, L. Tumanovska, A. Dorovskych, V. Lysenko, V. Tertykh, Y. Bolbukh, V. Dosenko, Anti-inflammatory and antioxidant effect of cerium dioxide nanoparticles immobilized on the surface of silica nanoparticles in rat experimental pneumonia, Biomed. Pharmacother. 92 (2017) 69–77, https://doi.org/10.1016/j.biopha.2017.05.064.